manuscript submitted to *JGR-Oceans*

G G G G G G G G - G G G G G G G G

Yanzhou Wei[1, 3, 4], Helen Pillar[1], Patrick Heimbach[1, 2*], An T. Nguyen[1], Gaël Forget[5] , Ou Wang[6], Ichiro Fukumori[6], Ian Fenty[6], and Martin Losch[7]

[1]Oden Institute for Computational Engineering and Sciences, University of Texas at Austin, Austin, TX, USA
[2]Jackson School of Geosciences, University of Texas at Austin, Austin, TX, USA
[3]State Key Laboratory of Satellite Ocean Environment Dynamics, Second Institute of Oceanography, Ministry of Natural Resources, Hangzhou, China
[4]Southern Marine Science and Engineering Guangdong Laboratory (Zhuhai), Zhuhai, China
[5]Massachusetts Institute of Technology, Cambridge, MA, USA
[6]Jet Propulsion Laboratory, California Institute of Technology, Pasadena, CA, USA
[7]Alfred-Wegener-Institut, Helmholtz-Zentrum für Polar- und Meeresforschung, Bremerhaven, Germany

*Corresponding author: Patrick Heimbach (heimbach@utexas.edu)

Key Points:

- Using a perturbed ensemble we explore the impact of uncertainty in atmospheric forcings on the ECCO ocean and sea ice state estimate.
- The ensemble yields alternative estimated solutions (acceptable model-data misfits) if time-mean forcing adjustments are retained.
- These alternative solutions are accompanied by moderate changes in climate relevant metrics, including ocean overturning and heat uptake.

Abstract

The Estimating the Circulation and Climate of the Ocean (ECCO) state estimate is the result of adjusting a set of controls comprising atmospheric forcings, initial conditions, and mixing parameters to reduce model-data misfits. Despite this, uncertainties remain in the solution. Among others, small amplitude perturbations to the optimized controls may yield differences in the estimated state without notably increasing the misfits, providing distinct but equally acceptable solutions to the inverse problem. We focus on the impact of uncertainty in the atmospheric controls via ensemble perturbation. Our multivariate EOF approach to construct the ensemble perturbations accounts for the covariance of control variables. Furthermore, it provides new insights into the space-time characteristics of (&&2M atmospheric adjustments. The two leading EOFs of these adjustments show a seasonal cycle dominated by high-latitude adjustments and a decadal component. Removing the time-mean of the adjustments results in large model-data misfits and thus unacceptable estimates. Ensemble perturbations in time-varying adjustments incur uneven uncertainties in oceanic metrics, e.g., in global meridional heat transport (0.03PW), the Atlantic meridional overturning circulation at 26°N (0.7Sv), or ocean heat uptake (15ZJ). These are an order of magnitude smaller than the uncertainty evaluated via ocean reanalysis intercomparisons and forward perturbation ensembles. The relatively weak impacts result from the relatively small amplitude of estimated atmospheric uncertainty in the ECCO release, which has undergone extensive optimization to reduce the model misfit to a massive set of observational constraints. Future work should assess the impact of other uncertainties, notably from the initial conditions and mixing parameters.

Plain Language Summary

Ocean reanalysis and state estimation seeks to bring an ocean model into consistency with available observations via data assimilation, providing a complete reconstruction of the time-evolving ocean state to support forecasting efforts and climate research. Uncertainty remains in the resulting products, however, arising from uncertainties in the underlying model, applied atmospheric forcings, assimilated data constraints, and assimilation method. Whilst computational challenges prevent comprehensive uncertainty quantification, this information is valuable for all applications (e.g., forecast initialization; robust climate change detection). To address this issue, we have sought to provide the first uncertainty estimate for the latest release of the ECCO global ocean and sea ice state estimate, spanning the period 1992-2017. Using an ensemble perturbation approach, we explore the impact of uncertainties in applied atmospheric forcings. Our ensemble design is advantageous in accounting for the joint variations between different atmospheric variables and in providing new insights into the space-time characteristics of adjustments made to these terms as part of the ECCO data assimilation procedure, highlighting the relative role of time-mean and time-variable adjustments. Our perturbed ensemble yields distinct solutions to the inverse problem with moderate changes in climate-relevant metrics, including ocean meridional overturning circulation, heat transport and heat uptake.

1 Introduction

For more than two decades, the Estimating the Circulation and Climate of the Ocean (ECCO) consortium has generated observationally constrained and dynamically consistent estimates of the

global ocean and sea ice states and accompanying parameters, supporting extensive investigations of the RFHDQV role in climate (Stammer et al., 2002; Forget et al. 2015a; Heimbach et al., 2019). The solution is produced via nonlinear least-squares optimization in which the model misfit to O(10^9) observations is successively reduced by making iterative gradient-based adjustments to a set of independent control variables. These controls comprise atmospheric forcings (varying in space and time), initial temperature, salinity, and velocity (varying only in space), and mixing parameters (varying only in space). Observational constraints include in-situ data from Argo profiling floats, ship-based Conductivity-Temperature-Depth (CTD) sensor and Expendable Bathythermograph (XBT), gridded temperature and salinity fields from the World Ocean Atlas, and high-latitude temperature (T) and salinity (S) acquisitions from Ice-Tethered Profilers (ITPs) and pinnipeds. These are complemented by satellite-based observations including mean dynamic topography (MDT), sea surface height anomalies (SSHA), sea surface temperature (SST), sea surface salinity (SSS), ocean bottom pressure (OBP) anomalies, and sea ice concentration (SIC) (Fukumori et al., 2020).

Despite extensive optimization, uncertainties remain in the adjusted controls, which are reflected in uncertainties in the estimated ocean and sea ice states. To date, however, no uncertainty estimate has accompanied the state estimates released. Whilst it is becoming increasingly common for unconstrained models to be released with some form of uncertainty estimate, mainly expressed in terms of ensembles (e.g., CESM Large Ensemble, Kay et al., 2015), this is still rare for model-data syntheses. Probabilistic ocean and sea-ice reanalyses employing four-dimensional variational data assimilation (DA) are typically limited to small ensembles (5 members for ECMWF ORAS5, Zuo et al., 2019). Regional, i.e., Arctic-focused efforts exist based on the Ensemble Kalman Filter (EnKF) approach that provide an uncertainty estimate via propagating the (Q.)V error covariance. Examples include the coupled ocean-sea ice DA system for the North Atlantic Ocean and Arctic, TOPAZ (Sakov et al., 2012) and EnKF-based surface ocean anomaly assimilation into the coupled Norwegian Climate Prediction Model (NorCPM, Counillon et al. 2016). In the absence of large single-framework ensembles, uncertainty in the reanalysed global ocean and sea-ice states has typically been assessed by comparison between different DA products (e.g., ORA-IP, Balmaseda et al., 2015; Utoila et al., 2018).

Broadly, sources of model uncertainties in the ECCO state estimate arise from uncertainties in (i) initial conditions, (ii) surface boundary conditions, i.e., atmospheric forcings and choice of bulk formulae to compute air-sea fluxes (although these SURMHFW strongly into parametric and structural model uncertainty), (iii) model parameters, in particular mixing, (iv) structural model error, including discretization errors (and errors arising from discretization truncation), and (v) bottom boundary conditions (e.g., model topography and geothermal heat fluxes) (e.g., Forget et al., 2015a). Observational uncertainties also contribute to uncertainty in the state estimate and are associated with measurement (or instrument) error, sampling errors arising from gaps in data coverage and aliasing, pre-processing errors, and uncertainties mapping between the observation and state space (i.e., observation-operator errors, e.g., -DQMH et al., 2017) for derived quantities.

The ECCO nonlinear inverse modeling framework is designed to adjust first-guess or prior estimates in uncertainties (i) - (iii) in order to bring the model into consistency with the observations within their assumed errors (accounting for observation and representation errors). These adjustments are applied iteratively and the optimization is halted when observational consistency is achieved and successive iterations cease to produce further reductions in model-data misfits. This final solution is then released

to the community. Given the uncertainties in both the priors of the input fields and the observations, however, alternative solutions to the inverse problem are expected that are statistically indistinguishable from the single deterministic solution released. Seeking such alternative solutions may be accomplished using ensemble methods, in which uncertain inputs are varied, leading to an ensemble of alternative solutions, i.e., solutions that retain a consistent model-data misfit in the sense described above. The ensemble spread in the solution as well as in salient diagnostics (e.g., key transport estimates or other ocean climate indices) then provides a measure of solution uncertainty.

In the context of the ECCO framework, one may consider perturbing initial conditions, model parameters, or atmospheric forcings. The task at hand is daunting, as it requires generation of an □ ensemble for each of these variables. In order to make initial progress whilst keeping the problem tractable, this work focuses on assessing the impact of atmospheric forcing uncertainties on the state estimate. These forcing uncertainties have been quantified by Chaudhuri et al., (2013) as the spread between different atmospheric reanalysis products. Subsequently, Chaudhuri et al., (2016) explored the extent to which these uncertainties could explain model-data differences by comparing the latter to the spread generated across an ensemble of single model experiments forced by different atmospheric reanalyses (also see Pillar et al., 2018). This study complemented the preliminary investigations by Forget and Ponte (2015) and Forget al., (2015a) into the sensitivity of the ECCOV4 solution to withholding various components, including the adjoint-based adjustments, from the atmospheric forcing.

A proper treatment of uncertainty in the ECCOV4 solution due to uncertainty remaining in the atmospheric forcing requires a thorough spatial and temporal characterization of the adjustments made to the atmospheric forcing controls, which has not yet been presented in detail. Here we provide this assessment before quantifying its impact. Importantly, we focus on the uncertainties remaining in the fully optimized atmospheric forcing from the latest ECCOV4 product (Release 4, ECCOV4r4), which are notably smaller than those considered in the investigations cited above.

The remainder of the paper is organized as follows. Our methods are presented in Section 2. Information is given on the ECCO Version 4 (ECCOV4) configuration and consecutive development cycles in Section 2.1, followed by a description of the empirical orthogonal function (EOF) decomposition of ECCOV4r4 adjustments and construction of the perturbation ensemble in Sections 2.2 and 2.3, respectively. In Section 3 we assess the atmospheric adjustments in ECCOV4r4, presenting their space-time characteristics and describing their dominant modes in Sections 3.1 and 3.2, respectively. Our main goal of providing initial estimates of ECCOV4r4 uncertainty is presented in Section 4, where we show the impact of time-mean and time-varying adjustments components on the simulated model-data misfits and estimated state in Sections 4.1 and 4.2, respectively. The paper concludes with a discussion of the implication of our results, study limitations and directions for future investigation.

2 Methods

2.1 ECCOV4 and control variable adjustments

ECCOV4 is configured at a nominal resolution of 1° on a [illegible] longitude-polar FDS (LLC, Forget et al., 2015) grid. The horizontal grid spacing varies from 22 km (at high latitude) to 110 km (at mid-

latitude) and telescopes to 40 km at the Equator. The vertical grid interval increases from 10 m near the surface to 457 m near the ocean bottom, with 50 vertical levels. Surface enthalpy fluxes are applied in ECCOV4 via the use of bulk formulae (Large and Yeager, 2009) whilst momentum fluxes are applied directly through specification of the wind stress. The nine atmospheric variables required to calculate these fluxes are surface air temperature (T_{air}), precipitation (P), specific humidity (q_{air}), zonal and meridional wind stress (τ_x, τ_y), downward longwave (R_{lw}) and net shortwave radiation (R_{sw}), wind speed (U), and sea level pressure (p) (Table 1). With the exception of U and p, all of these variables are adjustable controls within ECCOV4r4. In the case of p, omission from the control set is because pressure loading was not used during optimization of ECCOV4r4. In the case of U, omission from the control set is because in the bulk formulae in which it is present (those for latent and sensible heat fluxes) it is multiplied by existing control variables (atmospheric humidity and near-surface temperature, respectively). U and p are applied as unadjusted or filtered versions, respectively, of ERA-Interim fields.

For each ECCOV4 release the remaining atmospheric variables are applied as follows. First guess fields are obtained from the ERA-Interim atmospheric reanalysis product (Dee et al., 2011), denoted $V_{ERA}(r, t)$ as a function of space r and time t, combined with a first guess of adjustments, δ_{bh} : NP, to the seven variables. A final set of adjustments, $V_{adj}(r, t)$, is then inferred as part of the ECCOV4 iterative, gradient-based optimization, yielding a set of ECCO forcing fields,

$$\delta \qquad \delta \qquad \delta \qquad (1)$$

which, when applied to the model, leads to a reduced model-data misfit. In Eq. (1) subscript i denotes the release number and $N(i)$ the last iteration number for that release. For the first release the adjustments are initialized to zero. For all subsequent releases, adjustments are initialized from the previous release:

$$\delta \qquad \delta \qquad (2)$$

Appreciating this technical detail is important when interpreting some of the results in Section 3. For simplicity we will drop the subscript i and the iteration number when referring to the adjustment fields, $V_{adj,}$ and the adjusted forcing, $V_{ECCO,}$ for the remainder of the paper.

The cost function to be minimized,

$$\qquad (3)$$

contains three distinct contributions. The first is the model-data misfit squared, weighted by the error covariance matrix **R**. This error covariance accounts for both uncertainty in all observations, **y**, and representation error in the simulated state, **x**. **E** is the mapping of the model state to the observed

quantities (i.e., all assimilated in-situ and satellite-based constraints). The second and third terms penalize deviation of the initial condition, $\mathbf{x}_0$, and time-varying control variables, $\mathbf{u}(t)$, respectively, from their first guess. This deviation is weighted by estimates of control uncertainty, **B** and **Q** (e.g., Stammer et al., 2002; Wunsch and Heimbach, 2007) and integrated over the full estimated period ($t \in [t_0\ t_f]$). In practice, the ECCOV4 synthesis also incorporates diffusive smoothing of the controls and model-data misfits via application of pre- and post-processors, respectively, accounting for spatial correlations. The reader is referred to Forget et al., (2015a) for detailed discussion of this implementation. For this study, the uncertainties specified for the atmospheric subset of the full control set are important. These have been estimated from the spread between different atmospheric reanalysis products (Chaudhuri et al., 2013). As with the other control weights, they are held constant during the iterative optimization.

Four official releases of ECCOV4 have been provided to date. The first and second releases (r1 and r2) span the period 1992-2011 (Forget et al., 2015a; 2016). The third release (r3) was extended to span the period 1992-2015 and incorporate more major updates, including an extended suite of observational constraints with some new data types, reformulation of the model-data misfit cost function, and modified control variables with accompanying weights. Importantly, r3 introduced the separation of time-mean and time-variable misfits and adjustments to atmospheric control variables, to better address both time-mean and time-dependent biases (Fukumori et al., 2017). During production of the fourth release (r4), the latest release publicly available at the time of writing, it was determined that the control separation hindered the optimization (by leaving the time-varying controls largely uncorrected), resulting in a reversion back to the original control formulation used by r1 and r2 (Fukumori et al., 2020). Additional updates in r4 included a further extension of the analysis period to 1992-2017, an extension of the assimilated constraints (without adding new data types), and further modification of the control weights to rectify constraint correlations (Fukumori et al., 2020). Hereafter r4 will be referred to as ECCOV4r4 and we will continue to use ECCOV4 to describe aspects of the configuration independent of the release.

2.2 Multivariate EOF Analysis of Atmospheric Adjustments

This study is a first step toward providing a comprehensive uncertainty estimate for an ECCO solution, here ECCOV4r4, limiting the source of uncertainty to the atmospheric forcing fields. As described above, the nonlinear inverse modeling framework yields a set of atmospheric adjustment fields, $V_{\mathrm{adj}}(r, t)$, which, when added to the raw reanalysis fields, $V_{\mathrm{ERA}}(r, t)$, leads to an improved solution of the simulated state, hence the state estimate. A key element of our approach is in deriving a set of forcing perturbations that are within the prior forcing uncertainties and yield acceptable, i.e., statistically indistinguishable solutions when applied to the model. The approach relies on a low-order representation of these adjustment fields via an empirical orthogonal function (EOF) decomposition that provides the dominant patterns of covariation between the atmospheric adjustment fields.

The EOF method (e.g., North, 1984) allows each space-time varying field, $V_{\mathrm{adj}}(\mathrm{r}, \mathrm{t})$, to be written as the product of spatial patterns $S_j(r)$ and corresponding principal components (PCs), $a_j(t)$:

$$V_{\mathrm{adj}}(r, t) = \sum a_j(t)\, S_j(r). \qquad (4)$$

Here, $a_j(t)$ and $S_j(r)$ denote the j-th temporal and spatial EOF modes, respectively, ordered according to their relative importance in explaining the total variance of $V_{\mathrm{adj}}(r, t)$. We re-grid V_{adj} to a coarser

spatial resolution with a latitude □ interval of 4° and a longitude interval of 4°FRV□ ½ - the scaling factor FRV□ 1/2 is used to avoid artificial variance introduced by dense grid points at high latitudes - before performing the EOF analysis on the seven atmospheric adjustment fields as follows. First, we remove their long-term averages, $V_0(r)$, before dividing by the square root of their globally integrated variance, so that each field has the same spatially integrated variance in the multivariate EOF analysis. All processed fields are combined for the EOF analysis to obtain spatial modes for each V_{adj} field on the 4° latitude × FRV□ 1/2 longitude grid and their corresponding joint PCs. Finally, each PC is normalized to have unit standard deviation, and each $V_{adj}(r, t)$ field on the ECCOV4 grid is regressed onto the PCs to obtain the corresponding spatial patterns, $S_j(r)$. Each adjustment field can now be written as the sum of a long-term mean, $V_0(r)$, and time-varying component $V_j(r, t) = a_j(t)S_j(r)$, where the latter is decomposed using the EOF analysis such that:

$$V_{adj}(r, t) = V_0(r) + V_1(r, t) + V_2(r, t) + \square \quad . \quad (5)$$

The atmospheric variables used in ECCOV4r4, $V_{ECCO}(r, t)$, to compute the surface forcings can now be written as the sum of the first-guess atmospheric fields, $V_{ERA}(r, t)$, the time-mean adjustments ($V_0(r)$), and the EOF decomposition of the time-varying adjustments, $V_j(r, t)$:

$$V_{ECCO}(r, t) = V_{ERA}(r, t) + V_0(r) + V_1(r, t) + V_2(r, t) + \square \quad . \quad (6)$$

2.3 Perturbed Ensemble Construction

To explore the impact of uncertainty in the atmospheric forcing on the ECCOV4r4 state estimate, we run an ensemble of seven perturbation experiments. All seven ensemble members will be compared to the official ECCOV4r4 release (integrated with the optimized atmospheric forcing, $V_{ECCO}(r, t)$). For clarity, this will be referred to as the control experiment (Exp_ECCO) below. The first ensemble member (Exp_ERA) is an ECCOV4r4 re-run with all ECCOV4r4 atmospheric adjustments removed, so that the applied atmospheric fields are given by the first-guess ERA-Interim fields, $V_{ERA}(r, t)$. For the remaining ensemble members, three critical constraints guide our ensemble design. The first is that applied perturbations should remain within the bounds of the total estimated atmospheric uncertainty (see right column of Fig. 1 and Chaudhuri et al. 2013). The second is that the applied perturbations should not generate solutions with significantly amplified cost functions that would be rejected by the optimization framework. This threshold is defined in Section 4.1. We highlight that this second constraint distinguishes our approach from the design of forecast ensembles (e.g., Leutbecher & Palmer, 2008) where maximum ensemble dispersion is sought. Whilst the remaining 6 experiments are constructed to satisfy the first constraint, inspection of their model-data misfit cost functions will determine whether these runs produce acceptable solutions to the inverse problem. A third consideration in our ensemble construction is that we seek to account for covariances between atmospheric control variables.

To address all of these factors, we use the multivariate EOF decomposition (Eq. (6)) to compute perturbations to the control adjustments as follows. In ensemble member Exp0 we withhold all time-mean adjustments, $V_0(r)$, so that the applied atmospheric fields are given by $V_{ECCO}(r, t) \pm V_0(r)$. For members Exp_j with j □1:5, the j-th EOF component of the time-varying adjustment is withheld from all fields so that the applied atmospheric fields are given by $V_{ECCO}(r, t) \pm V_j(r, t)$ (Table 2). Since the top 5 EOF modes will be shown below to explain a significant fraction (~40%) of the total adjustment

variance, we do not explore the removal of higher order modes, which will have a less noteworthy impact on the ECCOV4r4 solution. We note that our method may also serve to increase the spread of our modest ensemble size, due to the orthogonality of the EOFs.

3 Results

3.1 Atmospheric Adjustment Characteristics

We show the time-mean and standard deviation of the atmospheric adjustments, V_{adj}, for each of the 7 atmospheric control variables (T_{air}, P, q_{air}, τ_x, τ_y, R_{lw}, R_{sw}), with their corresponding uncertainties in Fig. 1. For all atmospheric adjustments, the standard deviation (Fig. 1, middle column) is amplified in regions where the time-mean (Fig. 1, left column) is large. Averaged over the multidecadal ECCOV4r4 period, V_{adj} is shown to be large at high latitudes for almost all atmospheric controls. Large uncertainty here (Fig. 1, right column), resulting from limited observational coverage (Chaudhuri et al., 2013), enables greater deviation from the first-guess fields, V_{ERA}, during optimization. Notably, high latitude T_{air} adjustments reach 1.5□ in the time mean, cooling SST around Antarctica and in the Eastern Arctic, while warming SST along the east coast of Greenland and in the Western Arctic, serving to correct misfits with respect to satellite observations of SIC.

At high latitude, low temperature limits atmospheric moisture content so that both the uncertainty and adjustment for rain, P, and specific humidity, q_{air}, are relatively low here (Fig 1. b, c, p, q). In contrast, q_{air} and P uncertainties are largest in the tropics and Inter-Tropical Convergence Zone (ITCZ), respectively, where substantial uncertainty in boundary layer dynamics and cloud microphysics yields large reanalysis spread (Chaudhuri et al., 2013). Large P and q_{air} adjustments in these regions are associated with a net drying effect, correcting known biases in ERA-Interim (see Fig. 23 in Dee et al., 2011). Substantial adjustments to shortwave radiation, R_{sw}, are also made over the ITCZ and eastern boundary upwelling systems, reaching 20 Wm^{-2} and acting to cool near-surface ocean temperature (Fig. 1g). This may reflect the projection of model error (i.e., spuriously weak and broad upwelling) onto the atmospheric forcing, as opposed to the removal of systematic R_{sw} biases. Adjustments in R_{sw} and T_{air} (Fig. 1a) drive time-mean cooling throughout most mid and low latitude regions, opposed by time-mean SST warming driven by adjustments to longwave radiation, R_{lw} (Fig. 1f). This compensating influence of R_{sw} and R_{lw} is not easily interpreted from the perspective of model bias correction and so likely reflects the removal of systematic biases in ERA-Interim.

To explore the temporal variability of the adjustments, we start by inspecting V_{adj} at a single location (40.7 °N, 67.5 °W) off the US eastern seaboard during the full ECCOV4r4 period (right column in Fig. 2), highlighting that adjustments covary between different atmospheric control variables on subseasonal to multiannual timescales. We also compare the evolution of V_{adj} with the unadjusted forcing, V_{ERA}, during a single year (1992, left column in Fig. 2) to demonstrate that the adjustments are an order of magnitude smaller than the unadjusted forcing for all controls. Inspecting the long-term evolution of V_{adj} at our selected site (right column in Fig. 2) reveals abrupt transitions in the temporal characteristics of the adjustments. For example, R_{lw} adjustments show abrupt termination of strong subseasonal variations after 2011 (Fig. 2m), and τ_x and τ_y adjustments are dominated by a weak seasonal cycle before 2002 but much stronger subseasonal variations thereafter (Figs. 2k&l). These

temporal characteristics of V_{adj} are not restricted to our chosen location, as shown in the time series of V_{adj} averaged over different ocean basins in Figs. 3-5.

Strong seasonal cycles in the high latitude regions are shown for control variables impacting the surface enthalpy flux (Figs. 5a, c, f, g). Precipitation adjustments vary in phase for all regions (Figs. 3-5b), which is due to the inclusion of global mean sea level and bottom pressure misfits in the ECCOV4r4 cost function (first introduced in r3, Fukumori et al., 2017). As for our single location (Fig. 2) there is an abrupt transition in V_{adj} for τ_x and τ_y in all basins to show stronger subseasonal variability after 2002 (Figs. 3-5d,e). This year marked the launch of GRACE, enabling assimilation of monthly OBP anomalies into ECCOV4r4 (first introduced in r3, Fukumori et al., 2017). Although there were other changes to the global ocean observing system at this time (e.g., new satellites for SSH and SST, Fukumori et al., 2017), it is likely that the introduction of a new data type, rather than new data streams, significantly impacted the optimization. Since seasonal variations in OBP are primarily related to fast barotropic dynamics poleward of the tropics (Gill & Niiler, 1973; Ponte, 1999), model misfits to these data in the extratropics are principally corrected by adjusting wind stress controls, explaining both why the 2002 transition is only seen for τ_x and τ_y and why it is weaker in the lower latitude integral (Fig. 3d,e). This result is also consistent with Köhl et al. (2012), who showed the largest impacts of OBP assimilation in the subtropical gyres and polar latitudes. Within the tropics, baroclinic dynamics exert a stronger influence on OBP (Gill and Niiler, 1973; Piecuch, 2013) and we expect the full control set to come into play in influencing stratification to reduce OBP misfits. We hypothesize that this spread of information from OBP observations across multiple controls, which are also adjusting to minimize other model-data misfits, explains why the OBP-driven 2002 transition is not seen in any controls except for the wind stress components in Fig. 3.

In all basins, V_{adj} for R_{lw} shows enhanced subseasonal variability before 2011 (Figs. 3-5f). This year is marked by the onset of widespread SSS assimilation (from Aquarius, Fukumori et al., 2017). If this is the underlying cause of the 2011 transition, however, it is not obvious why the transition is not also seen in V_{adj} for P, since P serves as a more effective control on SSS. We also explored whether this enhanced subseasonal variability could arise from the separation of time-mean and time-dependent adjustments moving from r2 (extending from 1992-2011) to r3 (extending from 1992-2015). The enhanced variability is, however, on timescales shorter than the adjustment period (14 days) and was inherited by r3. At this time, the origins of this high frequency variability (introduced during r1 or r2 production) remains unresolved.

3.2 Dominant Modes of Atmospheric Adjustment

The spatial and temporal variability patterns from the multivariate EOF analysis of the atmospheric adjustment fields are now examined. Figure 6 shows the variance explained by individual EOF modes and their accumulation. The first and second EOF modes explain approximately 13% and 11% of the total variance, respectively (Fig. 6a). Approximately 40% (63%) of the total variance is explained by top five (twenty) EOF modes cumulatively (Fig. 6b).

The first two EOF modes are shown in Figs. 7-8. The PC of the first EOF mode (V_1, Fig. 7) is dominated by the annual cycle, indicating this mode serves to correct seasonal variability in the first-guess atmospheric fields. Strong annual variability was shown to be a prominent feature in the total adjustment fields (Figs. 3-5), and their variation patterns (Fig. 7) are consistent with the spatial patterns

of standard deviations of V_{adj} (middle column in Fig. 1). The PC of V_1 displays a decreasing amplitude after the year 2011, which was noted earlier for the full adjustments in T_{air} at low latitudes (Fig. 3a). The spatial patterns of V_1 for R_{lw} and R_{sw} adjustments (Fig. 7) are similar and vary in phase, with the latter having a larger amplitude, consistent with those shown in Figs. 3-5. Large positive values over the Southern Ocean suggest a need to increase R_{lw} and R_{sw} during austral summer and to decrease it during austral winter compared to the first-guess fields. Also notable are negative values over the eastern subtropical portions of the basins during austral summer, coincident with regions of strong wind-driven upwelling. The net effect is SST and shallow subsurface warming over the eastern boundary upwelling regions and cooling over the Southern Ocean in austral summer. This effect reinforces that from T_{air} adjustments, which cool SST within the southern reaches of the Southern Ocean during the austral summer. Also prominent are hemispheric anomalies in q_{air} with negative values in the Southern Hemisphere and positive values in the Northern Hemisphere during austral summer. This serves to drive increased (reduced) upward latent heat flux during summer (winter) in each hemisphere and a suppression of associated SST seasonality.

The PC of the second EOF mode (V_2, Fig. 8) of the atmospheric adjustment fields exhibits a noteworthy decadal change. Following mainly constant, slightly negative values during the initial portion of the estimation period, the PC increases markedly to positive values from 2006 onward, tapering off and slightly reversing after 2014. A weak seasonal variability is superimposed on these interannual variations. This mode is principally focused in the polar regions for all atmospheric adjustment fields except P and q_{air}, for which it is amplified in the subtropical oceans. It is likely related to the combined effect of inhibited oscillations of τ_x and τ_y adjustments before 2002 (Figs. 4-5d, e) and decadal variability that was most notable for P in many regions (Figs. 3-5).

4. Impacts of Atmospheric Uncertainty on the State Estimate

Having characterized the spatial and temporal patterns of the adjustment fields via a low-order representation, we now investigate their influence on the state estimate. As described in Section 2.3, our approach is to withhold the time-mean adjustments and the five leading EOF modes of the time-varying adjustments in turn, to quantify the relative importance of correcting time-mean and time-varying biases in the first-guess atmospheric forcing whilst also providing initial estimates of the impact of remaining atmospheric uncertainty on the ECCOV4r4 solution. We start by discussing the spread in the model-data misfit across the perturbed ensemble (Section 4.1) before examining the spread in estimated ocean and sea ice states (Section 4.2). Following Nguyen et al. (2021), we will refer to [illegible] as the dimensional model minus data difference, [illegible] as the misfit scaled by the respective uncertainty (dimensionless), and [illegible] as the square of the normalized misfit (dimensionless).

4.1 Impacts of Atmospheric Uncertainty on Model-Data Misfits

As expected, the cost function (Eq. (3)) is smallest for the control experiment, Exp_ECCO, and largest in Exp_ERA (64.8% increase relative to Exp_ECCO; Fig. 9), in which the forcing is reverted back to the first-guess ERA-Interim fields. The cost function increase relative to Exp_ECCO for all remaining experiments varies between 0.5% and 21.3% (Fig. 9), with the largest increase seen in Exp0, indicating that time-mean adjustments are critical to the success of the optimization. To determine which

ensemble members provide an acceptable fit to the assimilated constraints, we examine normalized misfits for the seven largest contributions to the total cost function in Fig. 10a. Normalized misfit values □ indicate that the solution is in agreement with the observations, given the assigned uncertainty (combined observational uncertainty and model representation error). Normalized misfits for these major datasets exceed 1 only in experiment Exp_ERA and only for SSS and OBP. We now compare the spatial structure of the time-mean model-observation misfits produced during each experiment, focusing on MDT, SST, and SSS across the ensemble (Fig. 11), calculated using the Radar Altimeter Database System (RADS), Reynolds, and Aquarius datasets, respectively (see Fukumori et al., 2020).

For Exp_ECCO, the MDT misfit (Fig. 11a) is less than 4.0 cm in most regions, except within the vicinity of the western boundary currents. This arises from the difficulty of representing the complex dynamic processes in these regions. Withholding all ECCOV4r4 atmospheric adjustments in Exp_ERA has a notable detrimental impact on the estimated MDT, amplifying misfits globally. Similar results are found when withholding the time-mean adjustments in Exp0. In contrast, withholding individual EOF modes from the adjustments (Exp1 to Exp 5) yields almost identical MDT misfits to Exp_ECCO (not shown). Figure 11 shows the long-term mean SST (second row) and SSS (third row) misfits in Exp_ECCO and the perturbation experiments, computed with respect to the Reynolds SST and Aquarius SSS satellite products. As above, Exp_ECCO is seen to be in agreement with the observations throughout the majority of the global ocean. Larger misfits to SST are seen within the western boundary currents, Norwegian and Barents Seas, and along the ACC downstream of Drake Passage. Exp_ECCO SSS misfits are also large there and extend throughout most coastal regions. SST and SSS misfits are also significantly amplified in the experiments forced with unadjusted ERA-Interim atmospheric fields (Exp_ERA). For SST, Exp_ERA misfits retain a similar spatial pattern to Exp_ECCO (i.e., representing a standing pattern of amplification). In contrast, Exp_ERA SSS misfits are significantly amplified throughout the ocean interior and change sign in many locations relative to Exp_ECCO.

Similar to MDT, experiments Exp_ERA and Exp0 produce comparable results, whilst Exp1 to Exp5 produce comparable results to Exp_ECCO. These results suggest that the long-term mean model-observation misfits in MDT, SST, and SSS are primarily corrected by time-mean forcing adjustments. This does not necessarily indicate systematic biases in the first-guess atmospheric fields, but instead indicates how ocean model error is projected into the atmospheric forcing by the adjoint. Although Exp1 to Exp5 contribute little to the misfit in the mean fields, they have an influence on the time-evolving fields. For instance, since the atmospheric adjustment withheld in Exp1 represents the annual variability, time evolution of SST (dimensional) misfits computed with respect to satellite-based estimates display stronger seasonal SST anomaly misfits in Exp1 relative to the control experiment Exp_ECCO (Figure 12). Similarly, because the atmospheric adjustment withheld in Exp2 represents decadal variability, decadal SST anomaly misfits are enhanced in Exp2 (Figure 12d).

4.2 Impacts of Atmospheric Uncertainty on Estimated Ocean & Sea Ice State

Having quantified the impact of time-mean and time-varying adjustment components on the model-data misfit structure, we now inspect their impacts on the estimated ocean and sea ice state. The differences in the long-term mean SST and SSS for the seven sensitivity experiments relative to those in Exp_ECCO are shown in Figs. 13 & 14. The differences in the long-term mean SIC relative to

Exp_ECCO are shown in Fig. 15 for Exp0 and Exp_ERA. As discussed above, the differences seen in Exp_ERA and Exp0 are major and widespread, altering pointwise SST, SSS, and SIC by up to 1°C, 1g/kg, and 0.1, respectively. Whilst withholding individual EOF modes from the adjustments was determined to only weakly amplify the cost function (by less than 10%, Fig. 9), appreciable changes in long-term mean SST and SSS are seen with conspicuous spatial structures in Exp1 to Exp5 (Fig. 14). Notably, Exp1 introduces SST warming of about 0.1°C around Antarctica and SST cooling of similar amplitude in the high latitudes of the Northern Hemisphere, accompanied by largely positive (negative) SSS change in the Southern (Northern) Hemisphere (Fig. 14). Exp2 introduces SST warming around Greenland and SSS freshening in much of the subtropical global ocean (Fig. 14). SST and SSS changes in Exp3 are concentrated in the polar regions and the ITCZ.

As shown in Fig. 9, withholding time-mean adjustments, V_0, leads to a significantly amplified costfunction. Although the model-data misfits remain within the applied uncertainty for key data sets when averaged globally (Fig. 10a), they exceed the applied uncertainty over large regions of the ocean interior (not shown) and would likely be rejected during the optimization. For this reason, we do not consider these time-mean components when quantifying the effect of remaining atmospheric uncertainties on the ECCOV4r4 solution, since they are essential in the success of the optimization. Instead, we quantify impacts of remaining atmospheric uncertainties from the spread of solutions generated in Exp1 to Exp5, for which resulting misfits were shown to remain consistent (within uncertainties) with the observations, both in a globally-averaged sense (Fig. 10a and when inspected regionally. Below we will refer to the ensemble as this subset of five experiments in which individual EOF modes were withheld from the adjustments.

The impact of remaining atmospheric uncertainty on SST and SSS is shown in Fig. 14 as the ensemble (Exp1 to Exp5) mean and standard deviation of the difference in these fields computed with respect to Exp_ECCO. Remaining atmospheric uncertainty generates the largest SST uncertainty (±0.1°C) in the polar regions and within the Pacific ITCZ. SSS uncertainty is largest (±0.1g/kg) in the Arctic and subtropics. These patterns are attributable to the uncertainty structure in the atmospheric reanalysis. That is, variables strongly impacting SST (e.g., T_{air} , R_{lw}, and R_{sw}) have larger uncertainties (including known errors) at high latitudes, whereas those directly influencing SSS (e.g., P) have larger uncertainties (including known errors) at low latitudes (see Chaudhuri et al., 2013 and right column of Fig. 1). Atmospheric uncertainty is shown to generate uncertainties in SIC of less than 0.1 everywhere. Largest SIC uncertainties are found at the sea ice edge (Fig. 15, fourth row), where complex physical processes occur and sensitivity to external forcing is large (e.g., Bidgeli et al., 2020).

The significant ensemble spread in SST, SSS, and SIC discussed above suggests that remaining atmospheric uncertainty may have important consequences for water mass transformation, overturning circulation, and the atmosphere-ocean partitioning and redistribution of heat in the climate system. To investigate this, we inspect the ensemble mean and spread for several commonly used oceanographic metrics of climatic relevance, including the global ocean meridional heat transport (MHT, Fig. 16), Atlantic meridional overturning circulation (AMOC, Fig. 17) streamfunction, time evolution of AMOC and Atlantic MHT at 26°N (Fig. 18), and global ocean heat uptake (OHU, Fig. 19).

The ensemble mean difference in global MHT is largest in the subtropics of both hemispheres. The sign of the ensemble mean difference indicates that poleward MHT is generally amplified in Exp1-Exp5. As seen from the depth-integrated MHT, the amplitude of the ensemble mean difference in MHT (about 0.005 PW) is approximately 0.3% of the MHT in Exp_ECCO (about 1.5 PW), which is

much smaller than the difference caused by different atmospheric forcing products (e.g., Fig. 15a, Forget and Ferreira, 2019). To put this in context, we highlight that MHT changes of approximately 10% are projected by the end of the 21st Century under weak forcing scenarios (RCP2.6, Mecking & Drijfhout, 2023). Additionally, we note that our estimated MHT uncertainty is much smaller than the uncertainty indicated by intercomparison of independent ocean reanalyses. Jackson et al., (2019) compared key circulation metrics across an ensemble of 11 ocean reanalysis products and showed that the amplitude of the ensemble spread is approximately 30-70% of the ensemble mean MHT throughout low- and mid-latitudes. In making these comparisons with our results, however, it is important to recall that reanalysis intercomparisons incorporate a much broader range of uncertainty sources than we investigate here, which explains the larger spread found in inter-reanalysis comparisons. Therefore, the comparatively small uncertainty reported in our study is not meant to imply improved quality. For completeness we also show the MHT change in Exp0 and EXP_ERA relative to Exp_ECCO. Although these solutions showed notable changes in surface circulation and buoyancy (Figs. 11 & 12), perturbations to MHT are remarkably small.

Atmospheric uncertainty in ECCOV4r4 also has a moderate impact on the time evolution of AMOC (Fig. 16). Removing the time-mean adjustment in the forcing (Exp0) causes a weakening of the deep overturning cell by roughly 1 Sv (10^6 m^3s^{-1}) and a strengthening of the shallow cell (above ~400 m). In contrast, the difference between ECCOV4r4 and the ensemble mean of the time-varying forcing experiments (Exp1 to Exp5) is much smaller (of the order of 0.1 Sv), suggesting only a weak impact of the EOF modes on the AMOC. Time series at 26°N show that MHT and MOC largely covary on interannual timescales across the ensemble (Fig. 17), consistent with the strong correlation observed between these two metrics (e.g., Johns et al., 2023). Atmospheric uncertainty results in MHT and MOC uncertainty on interannual to decadal timescales. Comparison of the MOCs and MHTs simulated with ECCO-adjusted atmospheric forcing and the initial unadjusted ERA forcing suggests that the ECCO assimilation acts to correct the declining trends in these climate metrics from the unconstrained simulation with ERA forcing. In Exp1 to Exp5, the maximum deviation from Exp_ECCO varies between -0.02 and 0.03 PW for MHT and between -0.5 to 0.7 Sv for MOC (representing changes of approximately 3% relative to mean values in Exp_ECCO). For context, this is an order of magnitude smaller than the spread assessed in intercomparisons of ocean reanalyses (e.g., approximately 5 Sv for AMOC at 26°N, Jackson et al., 2019). It is also an order of magnitude smaller than the uncertainty estimated using single model ensembles subject to forcing from different atmospheric reanalyses (Brodeau et al., 2010, He et al., 2016, Chaudhuri et al., 2016, Pillar et al., 2018). Importantly, these single model ensembles were not executed in an optimization framework, so no assessment was made as to whether applied perturbations produced ocean states consistent with available observations.

The ensemble mean differences are positive for almost all years spanned by the state estimate, indicating that the AMOC is generally amplified in Exp1-Exp5. Ensemble spread in MHT and MOC is accompanied by significant spread in OHU estimates reaching 15 ZJ, approximately 10% of the OHU in Exp_ECCO (Fig. 18). This is an order of magnitude smaller than the estimated total OHU uncertainty (Zanna et al., 2019). Removing the time-mean atmospheric forcing (Exp0) produces an OHU which follows the ECCOV4r4 estimates up to 2005 but begins to deviate thereafter. This timing appears to coincide with the timing of principal component 2 (Fig. 8h). In turn, the solution from the unadjusted solution (Exp_ERA) deviates from ECCOV4r4 during the first half of the estimation period

but then catches up with ECCOV4r4 during the second half. This suggests that EOF2 may contribute to adjusting the full solution to a decadal mode of variability, occurring around 2005.

5 Discussion & Conclusions

The ECCO ocean and sea ice state estimate is a dynamically consistent model-data synthesis, providing an invaluable tool for climate research. Consecutive releases of this product have each undergone extensive adjoint-based optimization to reduce the model-data misfits by adjusting a set of controls comprising atmospheric forcings, initial conditions, and ocean mixing parameters. Although the optimized ocean and sea-ice states have been extensively documented and explored in the literature, little attention has been given to the nature of the control variable adjustments to date. Similarly, no comprehensive estimate has to date been offered for the impact of uncertainty remaining in the adjusted controls on the solution. Here, we have sought to provide both an assessment of the space-time characteristics of ECCOV4r4 control adjustments and an initial estimate of the impact of their uncertainty on the simulated ocean and sea-ice state. We have focused on the atmospheric subset of the ECCOV4r4 control set, which facilitated both objectives by allowing adjustment covariances to be more easily accounted for and avoiding the complexity of assessing interactions between surface and interior sources of uncertainty.

In the first part of our study, we explored the nature of the adjustments made to the seven atmospheric control variables. For most atmospheric controls, the time-mean adjustments are largest for the data-sparse high latitude regions (Fig. 1). Specific humidity and precipitation adjustments are, however, largest in the tropics and ITCZ, respectively, and shortwave radiation adjustments are also large there and over the eastern boundary upwelling systems. By construction, these distributions are largely shaped by patterns of atmospheric uncertainty applied in the optimization framework (Fig. 1) and have been discussed in detail by Chaudhuri et al. (2013).

Inspection of temporal variations in ECCOV4r4 adjustment fields reveals some intriguing characteristics, including abrupt transitions in both their pointwise (Fig. 2) and spatially integrated (Figs. 3-5) evolution over the estimated period. These transitions are associated in part with extensions to the global observing system, as also seen in other data-assimilating products (e.g., ERA5, Hersbach et al., 2020). However, they are also caused by past changes to the optimization machinery (i.e., model-data misfit and atmospheric control splitting into time-mean and varying components) as well as other release updates. These artifacts are propagated through consecutive ECCO releases due to the practice of initializing atmospheric adjustments with those from the previous release (Eq. (2)). These findings encourage a clean start (i.e., adjustment initialization to zero) for the next ECCO production cycle.

Further investigation of the time-varying atmospheric adjustments and their covariance was facilitated by multivariate EOF analysis. The rationale for considering a multivariate EOF is that physics-based covariation among different atmospheric state variables should be accounted for in realistic perturbation experiments. Whilst the first EOF mode serves to correct seasonal variability in the first-guess atmospheric forcing (Fig. 7), the second mode adjusts a decadal change that occurs in about 2005 (Fig. 8). To explore the relative importance of the time-mean atmospheric adjustments and the top five EOF modes which explain 40% of the total variance, we executed a seven-member forward

perturbation ensemble. In six members, we withheld each of these six adjustment components, in turn, from the fully optimized forcing (Exp0 to Exp5). In the final member (Exp_ERA), all ECCOV4r4 adjustments were withheld from the forcing. Exp0 and Exp_ERA yielded comparable results, indicating that the time-mean adjustments are critical in reducing the model-data misfit. This may reflect removal of systematic ERA-Interim biases (e.g., suggested for large scale adjustments to R_{lw} and R_{sw} with opposing impacts on SST) or projection of model error into the time-mean controls (e.g., suggested for R_{sw} adjustments over spuriously weak eastern boundary upwelling regimes), or both. Withholding individual EOF modes (Exp1-Exp5) also yielded detectable differences in the estimated ocean and sea ice states (Figs. 13-14), but without significantly amplifying the cost function (Figs. 9 & 10).

In the final part of our study, we took advantage of these distinct yet acceptable solutions to the inverse problem to provide an initial estimate of uncertainty in the ECCOV4r4 solution from the Exp1-Exp5 ensemble spread. Since the ECCO state estimation framework is particularly well-suited to the detection and attribution of climate change (e.g., Wunsch and Heimbach 2013; Stammer et al., 2016, Wunsch et al., 2023), we focused on exploring uncertainty in climate-relevant metrics, including the global ocean meridional heat transport (Fig. 15 & 17), Atlantic meridional overturning circulation (Fig. 16 & 17), and net ocean heat uptake (Fig. 18). In each case, the uncertainty generated amounts to approximately 10% of that estimated in previous studies based on ocean reanalysis intercomparisons (Jackson et al.,2019) and forward perturbation ensembles (Brodeau et al., 2010, He et al., 2016, Chaudhuri et al., 2016, Pillar et al., 2018). Importantly, our analysis differs from these previous investigations by focusing on uncertainty remaining in the atmospheric forcing of ECCOV4r4, which has already undergone extensive optimization to reduce the model misfit to $O(10^9)$ observational constraints. This remaining uncertainty is, therefore, estimated to be considerably smaller than that evaluated in previous investigations, which incorporated a broader range of error sources and/or had no quantitative criterion for what remained an DFFHSWDEKROXWLRQ to the ocean inverse problem (see Fig. 10a).

Our ensemble construction served the dual purpose of (1) providing new insights into the space-time characteristics of control adjustments in ECCOV4r4, and (2) offering an initial assessment of the ECCOV4r4 solution uncertainty whilst accounting for covariation between control variables. Although our approach was also advantageous in balancing enhancement (via EOF orthogonality) and suppression of the ensemble dispersion, a fully comprehensive assessment of ECCOV4r4 solution uncertainty demands increasing both the ensemble size and perturbation amplitude in future work. Removal of the adjustment linear trend and seasonal cycle before performing the EOF decomposition could also be explored to determine if this would further aid interpretation of results.

Exploring the impacts of other sources of uncertainty, particularly that remaining in the initial condition and ocean mixing parameters, is another critical avenue for future work. The importance of ocean mixing parameter adjustments in ECCOV4 was demonstrated by Forget et al. (2015a) to overwhelm the impact of surface forcing adjustments in the optimization. Forget et al. (2015b) further highlighted the outsized importance of eddy parameter adjustments for removing long-term drifts in the ocean state. No distinction was made, however, between mixing adjustments that lead to acceptable solutions (in terms of normalized model-data misfit) and those that warrant further optimization. This encourages rigorous investigation of the impacts of uncertainty associated with these time-invariant

controls. Similarly, decadal predictions show strong dependence on initialization, particularly the choice of subsurface conditions at high latitude (e.g., Pohlmann et al., 2009, Dunstone & Smith 2010, Corti et al., 2015), where density perturbations may efficiently excite variability in the MOC (Zanna et al., 2011). Exploring this strong sensitivity to initial condition uncertainty in future work will be important for probing phase space more broadly, to determine if the ECCOV4r4 solution is the absolute global minimum (i.e., true optimal solution of the inverse problem). Finally, previous dedicated investigations have highlighted that bulk formulae uncertainty (e.g., choice of bulk transfer coefficients, use of bulk SST vs skin temperature) can have climatologically significant impacts on the simulated ocean state, including MHT (Bonino et al., 2022), and OHU (Brodeau et al., 2017, Yu 2019). We anticipate that much of this uncertainty is currently absorbed into (&&2M atmospheric states adjustments, which could be investigated in future work.

Potential approaches for investigating these sources of uncertainty include running perturbed parameter ensembles (e.g., Murphy et al., 2004; Deser et al. 2020) and modifying deterministic parameterization schemes to include time-dependent stochastic perturbations (e.g., Cooper and Zanna, 2015; Davini et al., 2017). Alternatively, adjoint-based methods available within ECCO may offer a useful opportunity to determine optimal perturbation patterns (e.g., Zanna et al., 2011; Amrhein et al., 2024) that could be leveraged to increase ensemble dispersion whilst retaining a tractable ensemble size. Future work will also address how best to combine impacts of uncertainty in atmospheric forcings, initial conditions and mixing parameters into a single uncertainty estimate to accompany future ECCO releases.

Acknowledgments

The authors have no conflict of interest to declare. HP, PH, ATN, and GF were supported, in part, by a Jet Propulsion Laboratory, California Institute of Technology (JPL/Caltech) Subcontract (&&2 - YW acknowledges support from the National Natural Science Foundation of China (41806024) and International Postdoctoral Exchange Fellowship Program (20190016) by the Office of China Postdoctoral Council. Part of this research was carried out at JPL/Caltech, under a contract with the National Aeronautics and Space Administration (80NM0018D0004). We thank ECCO collaborators for producing and distributing the solutions, source code, and analysis tools used in this study. We are grateful to Timothy Smith for providing a faster MHT calculation program in Python.

Open Research

The ECCOV4r4 solution and model configuration is available from https://data.nas.nasa.gov/ecco/data.php with accompanying instructions for re-runs provided by Wang et al. (2020).

References

Amrhein, D.E., Stephenson, D. and Thompson, L. (2024). A Dynamics-Weighted Principal Components Analysis of Dominant Atmospheric Drivers of Ocean Variability with an Application to the North Atlantic Subpolar Gyre. Journal of Climate, 37(8), 2673-2693.

Balmaseda, M. A., Hernandez, F., Storto, A., Palmer, M. D., Alves, O., Shi, L., ... & Gaillard, F. (2015). The ocean reanalyses intercomparison project (ORA-IP). Journal of Operational Oceanography, 8(sup1), s80-s97.

Bigdeli, A., Nguyen, A. T., Pillar, H. R., Ocaña, V., & Heimbach, P. (2020). Atmospheric warming drives growth in Arctic Sea ice: A key role for snow. Geophysical Research Letters, 47(20), e2020GL090236.

Bonino, G., Iovino, D., Brodeau, L., and Masina, S. (2022). The bulk parameterizations of turbulent air–sea fluxes in NEMO4: the origin of sea surface temperature differences in a global model study. Geosci. Model Dev., 15, 6873–6889.

Brodeau, L., B. Barnier, A. Treguier, T. Penduff, and S. Gulev, (2010): An ERA40-based atmospheric forcing for global ocean circulation models. Ocean Modell., 31, 88–104.

Brodeau, L., Barnier, B., Gulev, S. K., and Woods, C. (2017). Climatologically significant effects of some approximations in the bulk parameterizations of turbulent air–sea fluxes. J. Phys. Oceanogr. 47, 5–28.

Chaudhuri, A. H., Ponte, R. M., Forget, G., & Heimbach, P. (2013). A comparison of atmospheric reanalysis surface products over the ocean and implications for uncertainties in air–sea boundary forcing. Journal of Climate, 26(1), 153-170.

Chaudhuri, A. H., Ponte, R. M., & Forget, G. (2016). Impact of uncertainties in atmospheric boundary conditions on ocean model solutions. Ocean Modelling, 100, 96-108.

Cooper, F. C. & Zanna, L. (2015). Optimisation of an idealised ocean model, stochastic parameterisation of sub-grid eddies. Ocean Modelling, 88(C), 38–53.

Counillon, F., Keenlyside, N., Bethke, I., Wang, Y., Billeau, S., Shen, M. L. & Bentsen, M. (2016). Flow-dependent assimilation of sea surface temperature in isopycnal coordinates with the Norwegian Climate Prediction Model. Tellus A, 68(0), 32437.

Corti, S., Palmer, T., Balmaseda, M., Weisheimer, A., Drijfhout. S., Dunstone, N., Hazeleger, W., Kröger, J., Pohlmann, H., Smith, D., von Storch, J-S., and Wouters, B., (2015). Impact of Initial Conditions versus External Forcing in Decadal Climate Predictions: A Sensitivity Experiment. Journal of Climate, 28, 4454–4470.

Davini, P., von Hardenberg, J., Corti, S., Christensen, H. M., Juricke, S., Subramanian, A., ... & Palmer, T. N. (2017). Climate SPHINX: evaluating the impact of resolution and stochastic physics parameterisations in the EC-Earth global climate model. Geoscientific Model Development, 10(3), 1383-1402.

Dee, D. P., Uppala, S. M., Simmons, A. J., Berrisford, P., Poli, P., Kobayashi, S., ... & Vitart, F. (2011). The (5(,QWHUL Preanalysis: Configuration and performance of the data assimilation system. Quarterly Journal of the royal meteorological society, 137(656), 553-597.

Deser, C., Lehner, F., Rodgers, K. B., Ault, T., Delworth, T. L., DiNezio, P. N., ... & Ting, M. (2020). Insights from Earth system model initial-condition large ensembles and future prospects. Nature Climate Change, 10(4), 277-286.

Forget, G., Campin, J. M., Heimbach, P., Hill, C. N., Ponte, R. M., & Wunsch, C. (2015a). ECCO version 4: An integrated framework for non-linear inverse modeling and global ocean state estimation. Geoscientific Model Development, 8(10), 3071-3104.

Forget, G., and Ponte, R. M., (2015). The partition of regional sea level variability. Progress in Oceanography, 137, 173-195.

Forget, G., Ferreira, D., & Liang, X. (2015b). On the observability of turbulent transport rates by Argo: supporting evidence from an inversion experiment. Ocean Science, 11(5), 839-853.

Forget, G., J.-M. Campin, P. Heimbach, C. N. Hill, R. M. Ponte, & C. Wunsch (2016), ECCO version 4: Second Release, http://hdl.handle.net/1721.1/102062.

Forget, G., & Ferreira, D. (2019). Global ocean heat transport dominated by heat export from the tropical Pacific. Nature Geoscience, 12(5), 351-354.

Fukumori, I., O. Wang, I. Fenty, G. Forget, P. Heimbach, and R. M. Ponte (2017), ECCO Version 4 Release 3, http://hdl.handle.net/1721.1/110380.

Fukumori, I., Wang, O., Fenty, I., Forget, G., Heimbach, P., & Ponte, R. M. (2020). Synopsis of the ECCO central production global ocean and sea-ice state estimate (version 4 release 4). Retrieved from https://ecco-group.org/docs/v4r4_synopsis.pdf.

Gill, A. E., and P. P. Niiler (1973). The theory of the seasonal variability in the ocean, Deep Sea Res. Oceanogr. Abstr., 20, 141–177.

He, Y.-C., H. Drange, Y. Gao, and M. Bentsen, 2016: Simulated Atlantic meridional overturning circulation in the 20th century with an ocean model forced by reanalysis-based atmospheric data sets. Ocean Modell., 100, 31–48.

Heimbach, P., Fukumori, I., Hill, C. N., Ponte, R. M., Stammer, D., Wunsch, C., □ Zhang, H. (2019). Putting it all together: Adding value to the global ocean and climate observing systems with complete self-consistent ocean state and parameter estimates. Frontiers in Marine Science. Frontiers Media S.A. https://doi.org/10.3389/fmars.2019.00055

Hersbach, H., Bell, B., Berrisford, P., Hirahara, S., Horányi, A., Muñoz-Sabater, J., □ Thépaut, J. N. (2020). The ERA5 global reanalysis. Quarterly Journal of the Royal Meteorological Society, 146(730), 1999–2049.

Jackson, L. C., Dubois, C., Forget, G., Haines, K., Harrison, M., Iovino, D., Kohl, A., Mignac, D., Masina, S., Peterson, K.A., Piecuch, C.G., Roberts, C.D., Robson, J., Storto, A., Toyoda, T., Valdivieso, M., Wilson, C., Wang, Y., and Zuo, H. (2019). The mean state and variability of the North Atlantic circulation: A perspective from ocean reanalyses. Journal of Geophysical Research: Oceans, 124, 9141–9170.

□ T., Bormann, N., Bocquet, M., Carton, J.A., Cohn, S.E., Dance, S.L., Losa, S.N., Nichols, N.K., Potthast, R., Waller, J.A., and Weston, P. (2018). On the representation error in data assimilation. Quarterly Journal of the Royal Meteorological Society, 144: 1257-1278.

Johns, W.E., Elipot, S., Smeed, D.A., Moat, B., King, B., Volkov, D.L., Smith, R.H. (2023) Towards two decades of Atlantic Ocean mass and heat transports at 1□ Philos Trans A Math Phys Eng Sci. 381(2262):20220188.

Kay, J. E., Deser, C., Phillips, A., Mai, A., Hannay, C., Strand, G., Arblaster, J., Bates, S., Danabasoglu, G., Edwards, J., Holland, M. Kushner, P., Lamarque, J.-F., Lawrence, D., Lindsay, K., Middleton, A., Munoz, E., Neale, R., Oleson, K., Polvani, L., and M. Vertenstein (2015). The Community Earth System Model (CESM) Large Ensemble Project: A Community Resource for Studying Climate Change in the Presence of Internal Climate Variability, Bulletin of the American Meteorological Society, 96, 1333-1349.

Köhl, A., Siegismund, F., and Stammer, D. (2012). Impact of assimilating bottom pressure anomalies from GRACE on ocean circulation estimates. J. Geophys. Res., 117, C04032.

Large, W., & Yeager, S. G. (2009). The global climatology of an interannually varying air–sea flux data set. Climate dynamics, 33, 341-364.

Leutbecher, M. & Palmer, T.N. (2008). Ensemble Forecasting. Journal of Computational Physics, 227, 3515-3539.

Mecking, J.V., and Drijfhout, S.S. (2023). The decrease in ocean heat transport in response to global warming. Nat. Clim. Chang. 13, 1229–1236.

0XUSK - %)HUQiQGH]-6XiUH]1., Keppie, J. D., & Jeffries, T. E. (2004). Contiguous rather than discrete Paleozoic histories for the Avalon and Meguma terranes based on detrital zircon data. Geology, 32(7), 585-588.
Nguyen, A. T., Pillar, H., Ocaña, V., Bigdeli, A., Smith, T. A., & Heimbach, P. (2021). The Arctic Subpolar Gyre sTate Estimate: Description and Assessment of a DWD(&RQVWUDLQHG Dynamically Consistent 2FHDQ(6HIce Estimate for 2002±2017. Journal of Advances in Modeling Earth Systems, 13(5), e2020MS002398.
North G R. 1984. Empirical orthogonal functions and normal modes. J Atmos Sci, 41: 879-887.
Piecech, C. G. (2013), Dynamics of satellite-derived interannual ocean bottom pressure variability in the western tropical North Pacific, J. Geophys. Res. Oceans, 118, 5117±5128.
Pillar, H.R., Johnson, H.L., Marshall, D.P., Heimbach, P., & Takao, S., (2018), Impacts of atmospheric reanalysis uncertainty on Atlantic overturning estimates at 25N. J. Climate., 31, 8719±8744.
Ponte, R. M. (1999). A preliminary model study of the large-scale seasonal cycle in bottom pressure over the global ocean. J. Geophys. Res. 104(c1), 1289-1300.
Sakov, P., Counillon, F., Bertino, L., Lisæter, K. A., Oke, P. R. & Korablev, A. (2012). TOPAZ4: an ocean-sea ice data assimilation system for the North Atlantic and Arctic. Ocean Science, 8(4), 633±656. https://doi.org/10.5194/os-8-633-2012
Stammer, D., Wunsch, C., Fukumori, I., & Marshall, J. (2002). State estimation improves prospects for ocean research. Eos, Transactions American Geophysical Union, 83(27), 289-295.
Uotila, P., Goosse, H., Haines, K., Chevallier, M., Barthélemy, A., Bricaud, C., ... & Zhang, Z. (2019). An assessment of ten ocean reanalyses in the polar regions. Climate Dynamics, 52, 1613-1650.
Wang, O., Fukumori, I., and Fenty, I. 2020: ECCO Version 4 Release 4 User Guide [dataset]. Retrieved from https://www.ecco-group.org/docs/v4r4_user_guide.pdf
Wunsch, C., & Heimbach, P. (2007). Practical global oceanic state estimation. Physica D: Nonlinear Phenomena, 230(1-2), 197-208.
Wunsch, C., & Heimbach, P. (2013). Two Decades of the Atlantic Meridional Overturning Circulation: Anatomy, Variations, Extremes, Prediction, and Overcoming Its Limitations. J. Climate, 26, 7167-7186.
Wunsch, C., Williamson, S. & Heimbach, P. (2023). Potential artifacts in conservation laws and invariants inferred from sequential state estimation. Ocean Science, 19(4), 1253±1275.
Yu, L. (2019). Global air±sea fluxes of heat, fresh water, and momentum: energy budget closure and unanswered questions. Annu. Rev. Mar. Sci. 11, 227±248.
Zanna, L., Heimbach, P., Moore, A. M., & Tziperman, E. (2011). Optimal excitation of interannual Atlantic meridional overturning circulation variability. J. Climate, 24(2), 413-427.
Zanna, L., Khatiwala, S., Gregory, J.M., Ison, J., & Heimbach, P. (2019). Global reconstruction of historical ocean heat storage and transport, Proc. Natl. Acad. Sci. U.S.A. 116 (4) 1126-1131.
Zuo, H., Balmaseda, M., Tietsche, S., Mogensen, K., & Mayer, M. (2019). The ECMWF operational ensemble reanalysis-analysis system for ocean and sea ice: a description of the system and assessment. Ocean Sci., 15, 779-808.

Figure Legends

Figure 1. Mean (left column) and standard deviation (middle column) of the ECCOV4r4 atmospheric adjustments (V_{adj} in Eq. (1)) during 1992-2017. From top to bottom: air temperature at 2m above the sea surface (T_{air}), precipitation (P), specific humidity at 2m above the sea surface (q_{air}), zonal wind stress (τ_x, positive westwards), meridional wind stress (τ_y, positive southwards), upward longwave radiation (R_{lw}), and net shortwave radiation (R_{sw}). The uncertainties (right column) are taken from Chaudhuri et al., (2013) as the time-mean spread between atmospheric reanalyses. This spread was computed after averaging the original 6-hourly products over 14-day intervals (Chaudhuri et al., 2013), which is the atmospheric control adjustment period employed in ECCO. Large weights correspond to low uncertainty (i.e., low reanalysis spread), penalizing deviation of atmospheric controls from the initial guess, thereby restricting adjustment (V_{adj} in Eq. (1)).

Figure 2. (Left column) Time evolution of the (red) initial unadjusted and (blue) final adjusted atmospheric forcing fields at 40.7 °N, 67.5 °W off the eastern U.S. seaboard during 1992. Time evolution of the (green) applied adjustments is also shown to highlight their small amplitude relative to the first guess forcing. (Right column) Time evolution of all atmospheric adjustments for the full ECCOV4r4 period (1992 to 2017).

Figure 3. Time evolution of ECCOV4r4 atmospheric adjustment fields averaged over the tropical and subtropical ocean basins from 1992 to 2017.

Figure 4. Time evolution of ECCOV4r4 atmospheric adjustment fields averaged over the mid-latitude ocean basins from 1992 to 2017.

Figure 5. Time evolution of ECCOV4r4 atmospheric adjustment fields averaged over the polar ocean basins from 1992 to 2017.

Figure 6. Percentage of total variance in the ECCOV4r4 atmospheric adjustments, $V_{adj,}$ explained by (left) individual EOFs and (right) summed EOFs, computed from a multivariate EOF analysis (see Section 2.2).

Figure 7. First EOF mode of the ECCOV4r4 atmospheric adjustment fields. The color panels indicate the spatial patterns and the time series indicates the first Principal Component (PC).

Figure 8. Second EOF mode of the ECCOV4r4 atmospheric adjustment fields. The color panels indicate the spatial patterns and the time series indicates the second Principal Component.

Figure 9. Percentage increase in cost function in the 7 perturbed ensemble members relative to the control experiment. The cost function is defined identically in all experiments (see Eq. (3)), in each case incorporating all misfits to the full suite of in-situ and satellite-based constraints used in the optimization of ECCOV4r4 (Fukumori et al., 2020).

Figure 10. (a) Squared normalized model-data misfits QRUPDOLHGRVWV (dimensionless) and (b) their percentage contribution to the total costfunction in ECCOV4r4 (Exp_ECCO) and the 7 member ensemble. In each case, only the 7 terms making the largest contributions to the total cost function are

shown (explaining 89-94% of the total cost across the ensemble). These are temperature (T) and Salinity (S) from Argo (Argo_TS), T from expendable bathythermograph (XBT_T), T and S from the World Ocean Atlas (WOA_TS), ocean bottom pressure from satellite (OBP), SST and SSS from satellite, and deficits in sea ice concentration compared to satellite-based estimates (Seaice_deconc). Normalized costs <1 indicate that the model is consistent with the data given the applied uncertainty. Due to uncertainty in these prior weights (R in Eq. (3)), however, it is common practice to define acceptable normalized costs as those □2.

Figure 11. Time-averaged misfits of the MDT(m, first row), SST (°C, second row) and SSS (g/kg, third row) in the control experiment Exp_ECCO (left panels) and the sensitivity experiments Exp_ERA (middle panels),and Exp0 (right panels).

Figure 12. Time evolution of SST misfit along 30°W in the control experiment Exp_ECCO (a) and the sensitivity experiments Exp_ERA (b), and Exp1 (c) and Exp2 (d).

Figure 13. The difference in long-term mean SST (°C, left panels) and SSS (g/kg, right panels) in the perturbation experiments Exp_ERA (first row) and Exp0 (second row) relative to the control experiment (Exp_ECCO).

Figure 14. The difference in long-term mean SST (°C, left panels) and SSS (g/kg, right panels) in the perturbation experiments Exp1 to Exp5(top five rows) relative to the control experiment (Exp_ECCO). And their ensemble mean (sixth row) and standard deviation (bottom row).

Figure 15. The difference in long-term mean sea ice concentration (SIC) in the experiments Exp_ERA (first row) and Exp0 (second row) relative to the control experiment (Exp_ECCO), and the corresponding Exp1-Exp5 ensemble mean (third row) and standard deviation (fourth row) of the long-term mean SIC differences.

Figure 16. Mean (upper left) and standard deviation (bottom left) of both the global ocean meridional heat transport (MHT) per unit depth and the depth-integrated MHT, calculated from the monthly averaged output in the control experiment (Exp_ECCO). The depth-integrated MHTs simulated in Exp_ERA (blue line) and Exp0 (green line) are superimposed in panel (a). The ensemble mean (upper right) and standard deviation (bottom right) of both the differences in MHT and depth-integrated MHT computed with respect to Exp_ECCO. Ensemble members Exp_ERA and Exp0 are omitted from this calculation, so that we consider only the experiments withholding individual EOF modes from the adjustments (Exp1 to Exp5) which yield acceptable solutions to the optimization problem.

Figure 17. Atlantic meridional overturning circulation (AMOC) simulated in Exp_ECCO (a), and the difference between Exp0 and Exp_ECCO (b). Ensemble mean and spread of the differences in AMOC from Exp1 to Exp5 are shown in panels (c) and (d).

Figure 18. Low-pass (19-point Hanning filter) filtered monthly Atlantic meridional heat transport (a, MHT) and Atlantic Meridional Overturning Circulation (c, MOC) at 26°N from the control experiment Exp_ECCO (red line), and perturbation experiments Exp_ERA (blue line) and Exp0 (green line). Ensemble mean (red) and spread (dashed blue) of the differences in MHT (b) and MOC (d). Ensemble members Exp_ERA and Exp0 are omitted from this calculation, so that we consider only the

experiments withholding individual EOF modes from the adjustments (Exp1 to Exp5) which yield acceptable solutions to the optimization problem.

Figure 19. (a) Global ocean heat uptake since 1992 estimated from the control experiment (Exp_ECCO, red), Exp_ERA (blue) and Exp0 (green), where a low pass filter (19-point Hanning filter) has been applied to omit the seasonal cycle for clarity. (b) Ensemble mean (red) and spread (blue) of the differences in ocean heat uptake in Exp1 to Exp5.

Table 1. The atmospheric forcing fields and their sign convention used in ECCOV4r4. Adapted from Wang et al. 2020.

1	air temperature at 2 m above sea surface	T_{air}	
2	precipitation	P	positive to increase sea level
3	specific humidity at 2 m above sea surface	q_{air}	
4	East-West component of wind stress	$_{x}$	positive from east to west
5	North-South component of wind stress	$_{y}$	positive from north to south
6	upward longwave radiation	R_{lw}	positive to decrease ocean temperature
7	upward shortwave radiation	R_{sw}	positive to decrease ocean temperature
8	wind speed	U	
9	sea level pressure	p	

Table 2. Cost function increase (%) relative to Exp_ECCO for the 7 member perturbation ensemble. Exp_ECCO is the ECCOV4r4 solution forced by the final adjusted atmospheric fields $V_{\mathrm{ECCO}}(r, t)$. Exp0 is forced by the initial unadjusted atmospheric fields, $V_{\mathrm{ERA}}(r, t)$, from ERA-Interim. The remaining 5 experiments are run with different components of the atmospheric adjustments, $V_{\mathrm{adj}}(r, t)$, withheld, as described in the right column. $V_0(r)$ is the time-averaged component and $V_i(r, t)$ is the contribution from the i-th EOF mode of the time-varying component of $V_{\mathrm{adj}}(r, t)$.

Experiment Name	**Applied Atm Fields**	**Cost function Increase (%) Relative to Exp_ECCO**	**Description**
Exp_ERA	V_{ERA}	64.8	All atmospheric adjustments withheld
Exp0	$V_{\mathrm{ECCO}} - V_0$	21.3	Time-mean atmospheric adjustments withheld
Exp1	$V_{\mathrm{ECCO}} - V_1$	2.3	1st EOF of time-varying adjustments withheld
Exp2	$V_{\mathrm{ECCO}} - V_2$	8.0	2nd EOF of time-varying adjustments withheld
Exp3	$V_{\mathrm{ECCO}} - V_3$	1.7	3rd EOF of time-varying adjustments withheld
Exp4	$V_{\mathrm{ECCO}} - V_4$	2.0	4th EOF of time-varying adjustments withheld
Exp5	$V_{\mathrm{ECCO}} - V_5$	0.5	5th EOF of time-varying adjustments withheld

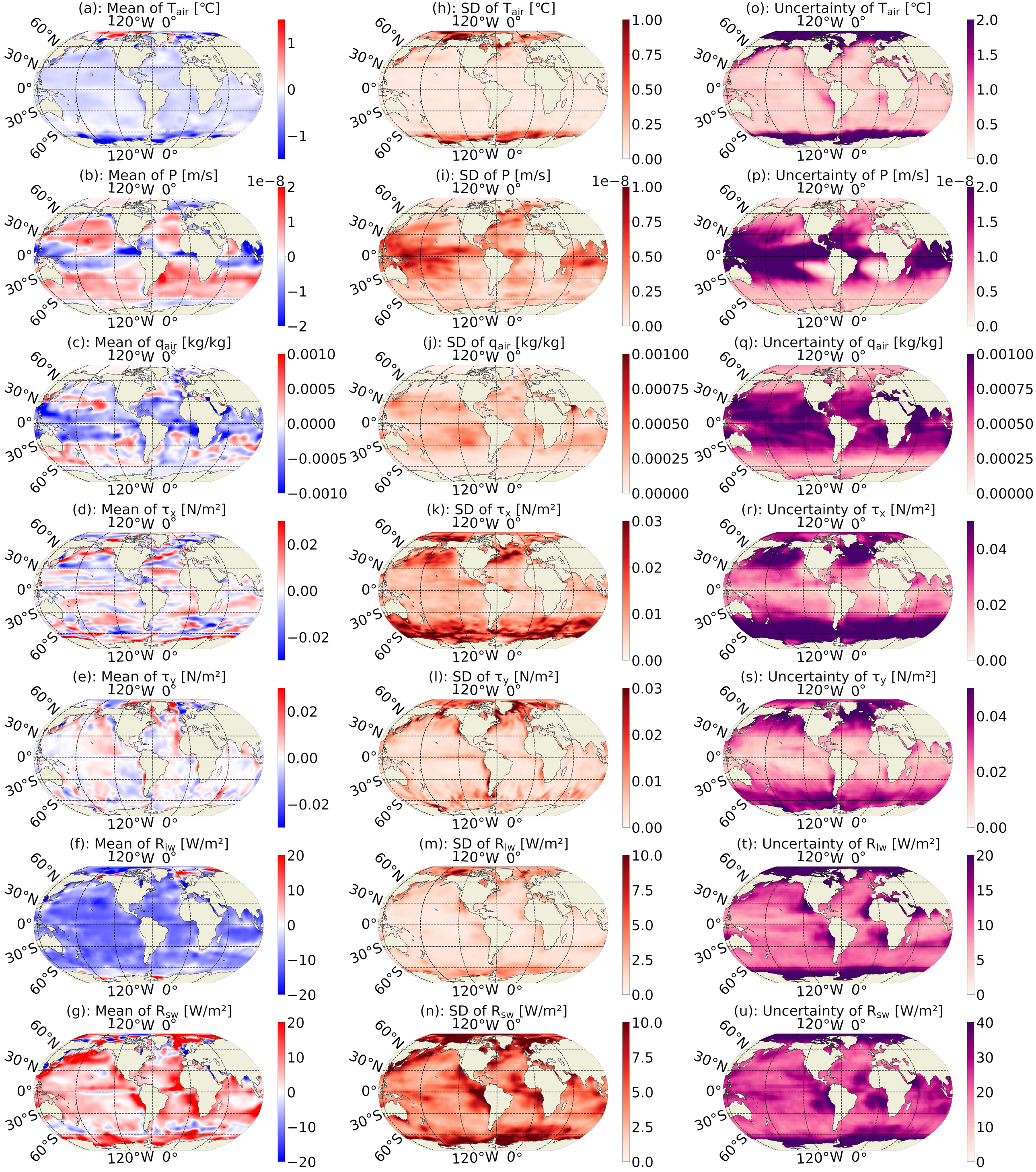
(a): Mean of T_{air} [°C]
(h): SD of T_{air} [°C]
(o): Uncertainty of T_{air} [°C]
(b): Mean of P [m/s]
(i): SD of P [m/s]
(p): Uncertainty of P [m/s]
(c): Mean of q_{air} [kg/kg]
(j): SD of q_{air} [kg/kg]
(q): Uncertainty of q_{air} [kg/kg]
(d): Mean of τ_x [N/m²]
(k): SD of τ_x [N/m²]
(r): Uncertainty of τ_x [N/m²]
(e): Mean of τ_y [N/m²]
(l): SD of τ_y [N/m²]
(s): Uncertainty of τ_y [N/m²]
(f): Mean of R_{lw} [W/m²]
(m): SD of R_{lw} [W/m²]
(t): Uncertainty of R_{lw} [W/m²]
(g): Mean of R_{sw} [W/m²]
(n): SD of R_{sw} [W/m²]
(u): Uncertainty of R_{sw} [W/m²]
120°W 0°
60°N
30°N
0°
30°S
60°S
1e−8

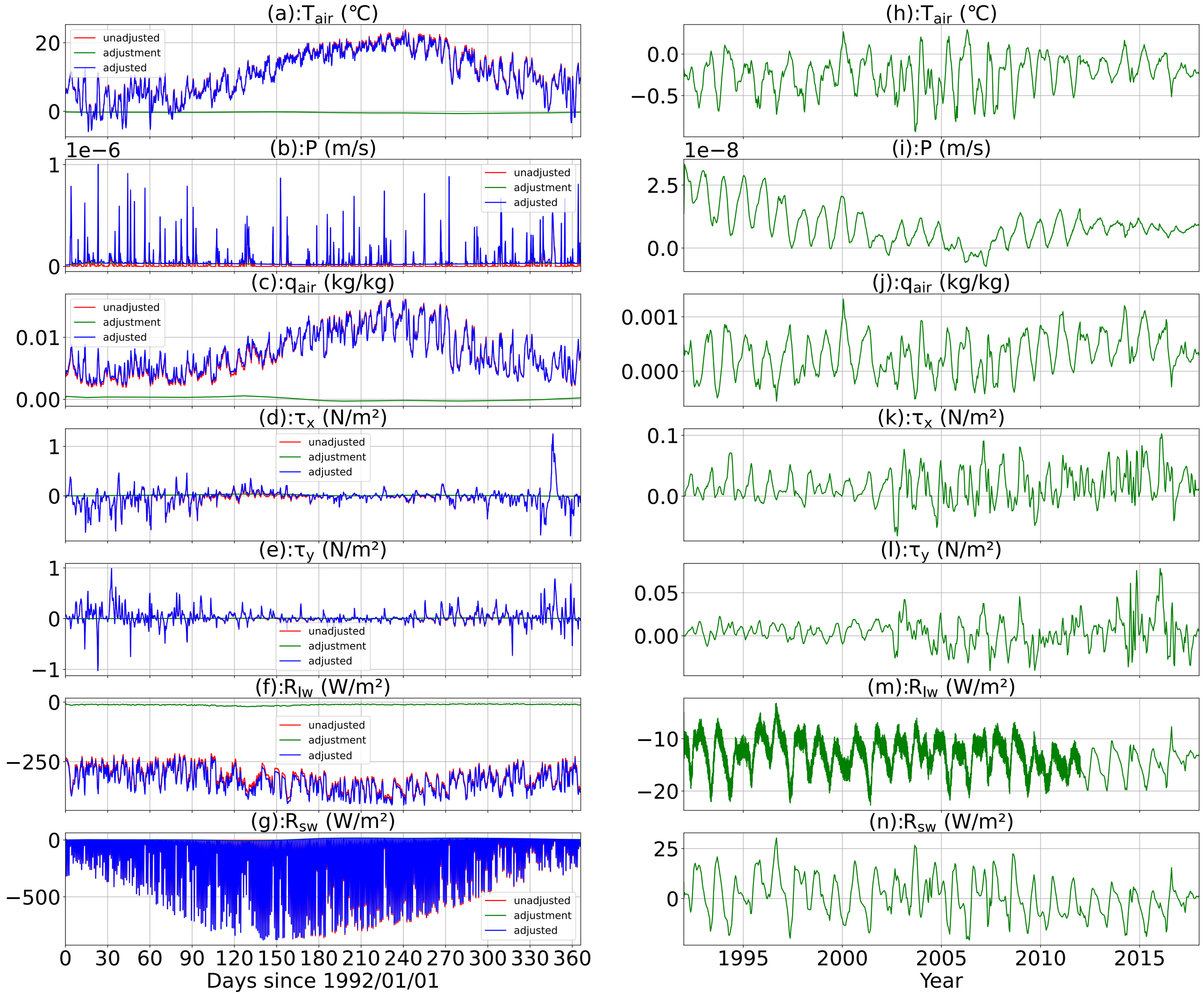
(a):T_air (°C)
(b):P (m/s)
1e−6
(c):q_air (kg/kg)
(d):τ_x (N/m²)
(e):τ_y (N/m²)
(f):R_lw (W/m²)
(g):R_sw (W/m²)
(h):T_air (°C)
(i):P (m/s)
1e−8
(j):q_air (kg/kg)
(k):τ_x (N/m²)
(l):τ_y (N/m²)
(m):R_lw (W/m²)
(n):R_sw (W/m²)
unadjusted
adjustment
adjusted
Days since 1992/01/01
Year

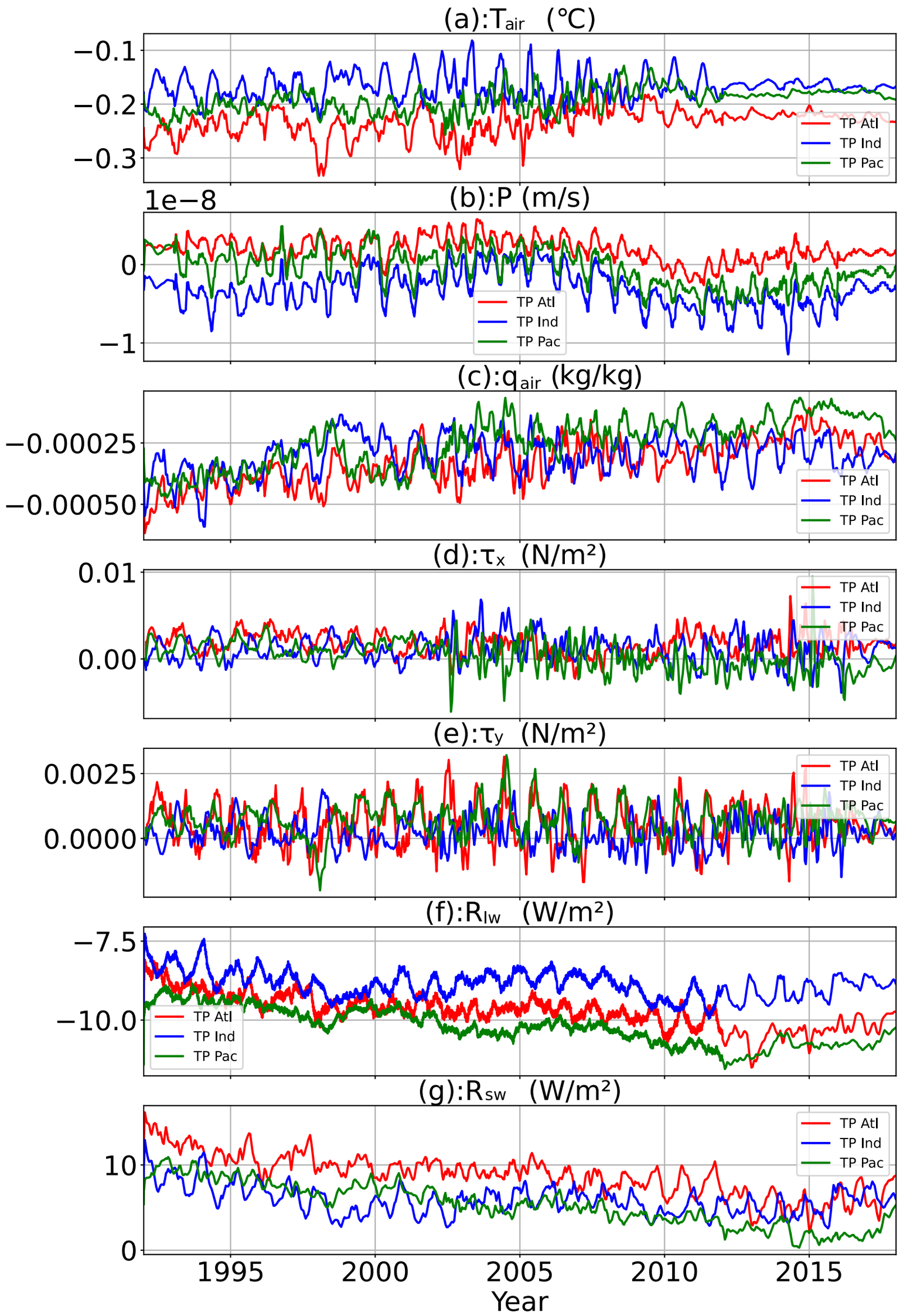
(a):T_air (°C)
−0.1
−0.2
−0.3
TP Atl
TP Ind
TP Pac
1e−8
(b):P (m/s)
0
−1
(c):q_air (kg/kg)
−0.00025
−0.00050
(d):τ_x (N/m²)
0.01
0.00
(e):τ_y (N/m²)
0.0025
0.0000
(f):R_lw (W/m²)
−7.5
−10.0
(g):R_sw (W/m²)
10
0
1995
2000
2005
2010
2015
Year

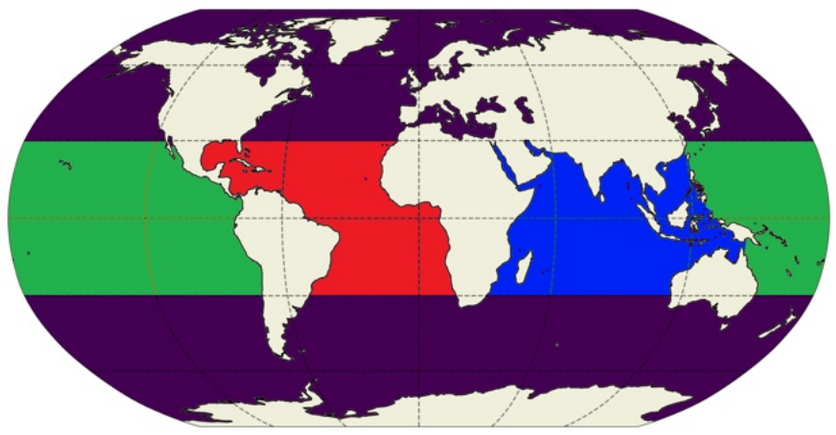

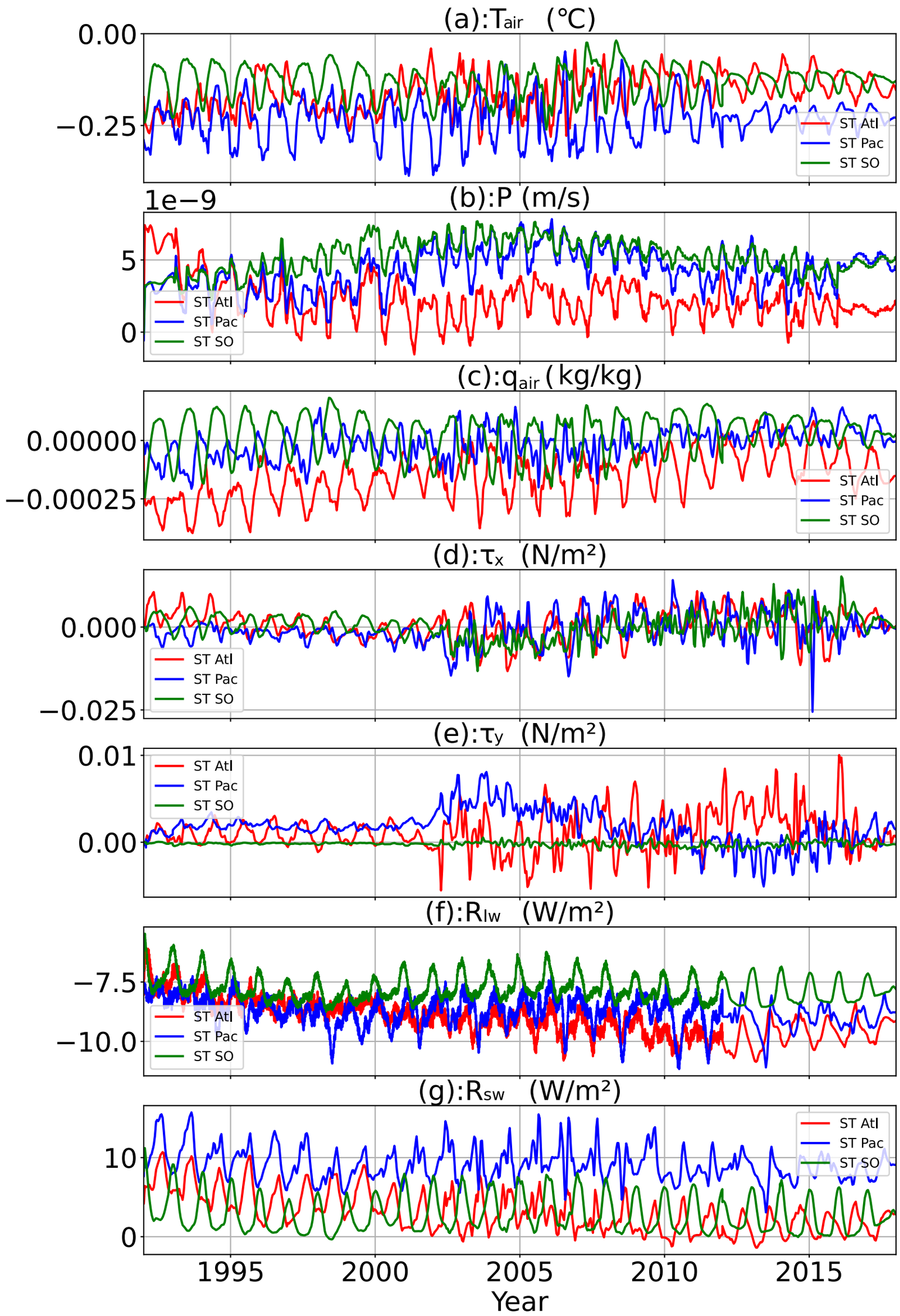
(a):Tair (°C)
0.00
−0.25
ST Atl
ST Pac
ST SO
1e−9
(b):P (m/s)
5
0
(c):qair (kg/kg)
0.00000
−0.00025
(d):τx (N/m²)
0.000
−0.025
(e):τy (N/m²)
0.01
0.00
(f):RIw (W/m²)
−7.5
−10.0
(g):Rsw (W/m²)
10
0
1995
2000
2005
2010
2015
Year

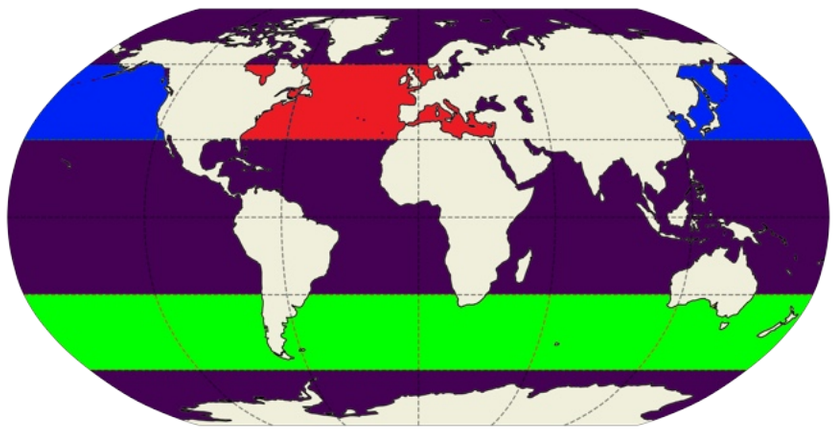

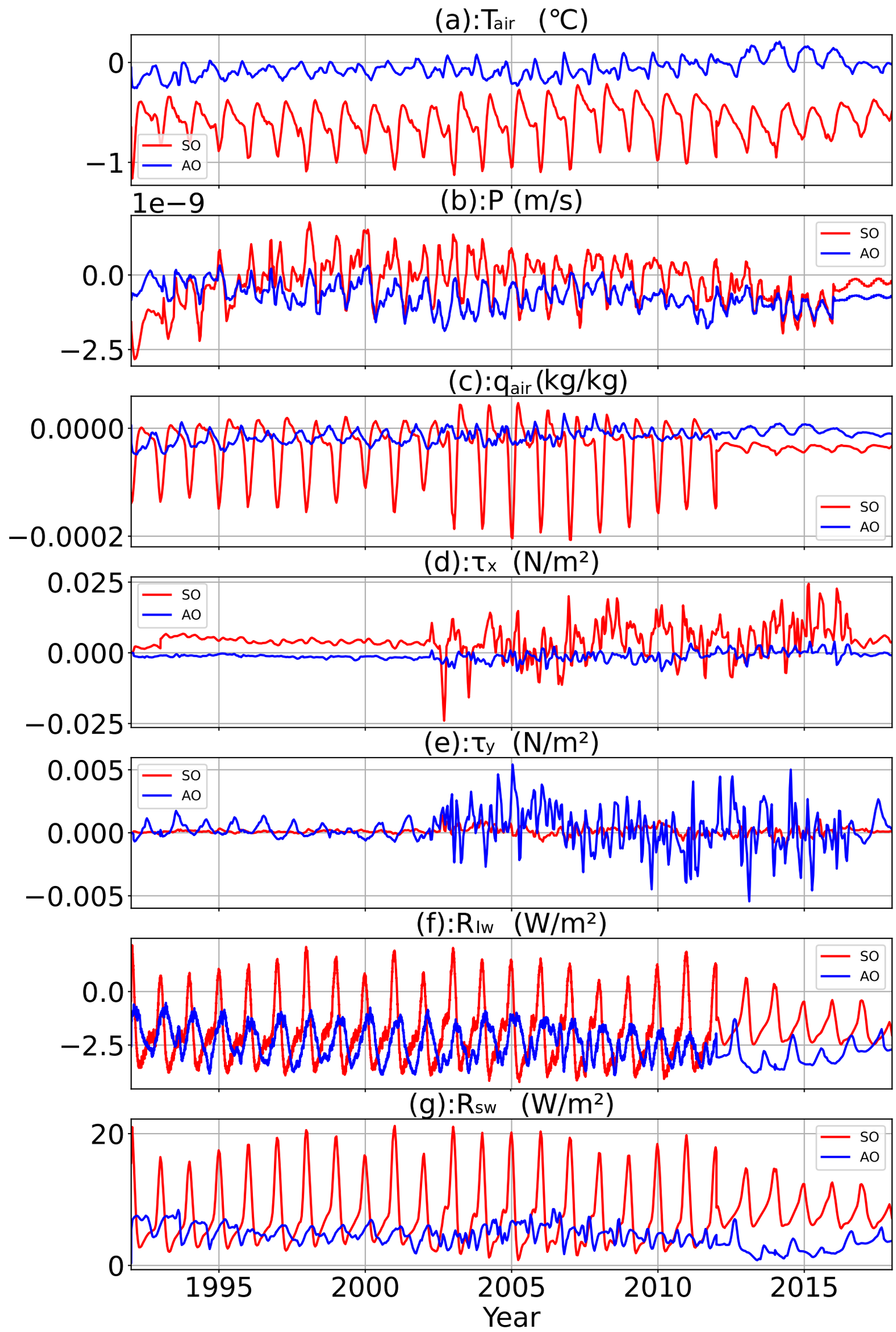
(a):Tair (°C)
0
−1
SO
AO
1e−9
(b):P (m/s)
0.0
−2.5
(c):qair (kg/kg)
0.0000
−0.0002
(d):τx (N/m²)
0.025
0.000
−0.025
(e):τy (N/m²)
0.005
0.000
−0.005
(f):Rlw (W/m²)
0.0
−2.5
(g):Rsw (W/m²)
20
0
1995
2000
2005
2010
2015
Year

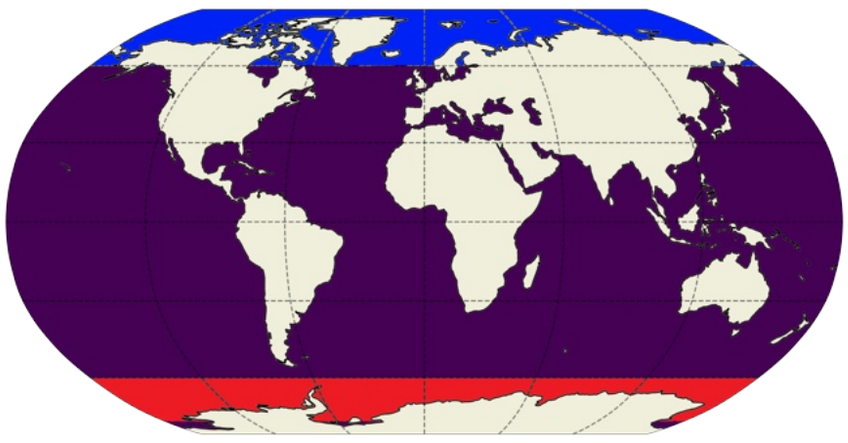

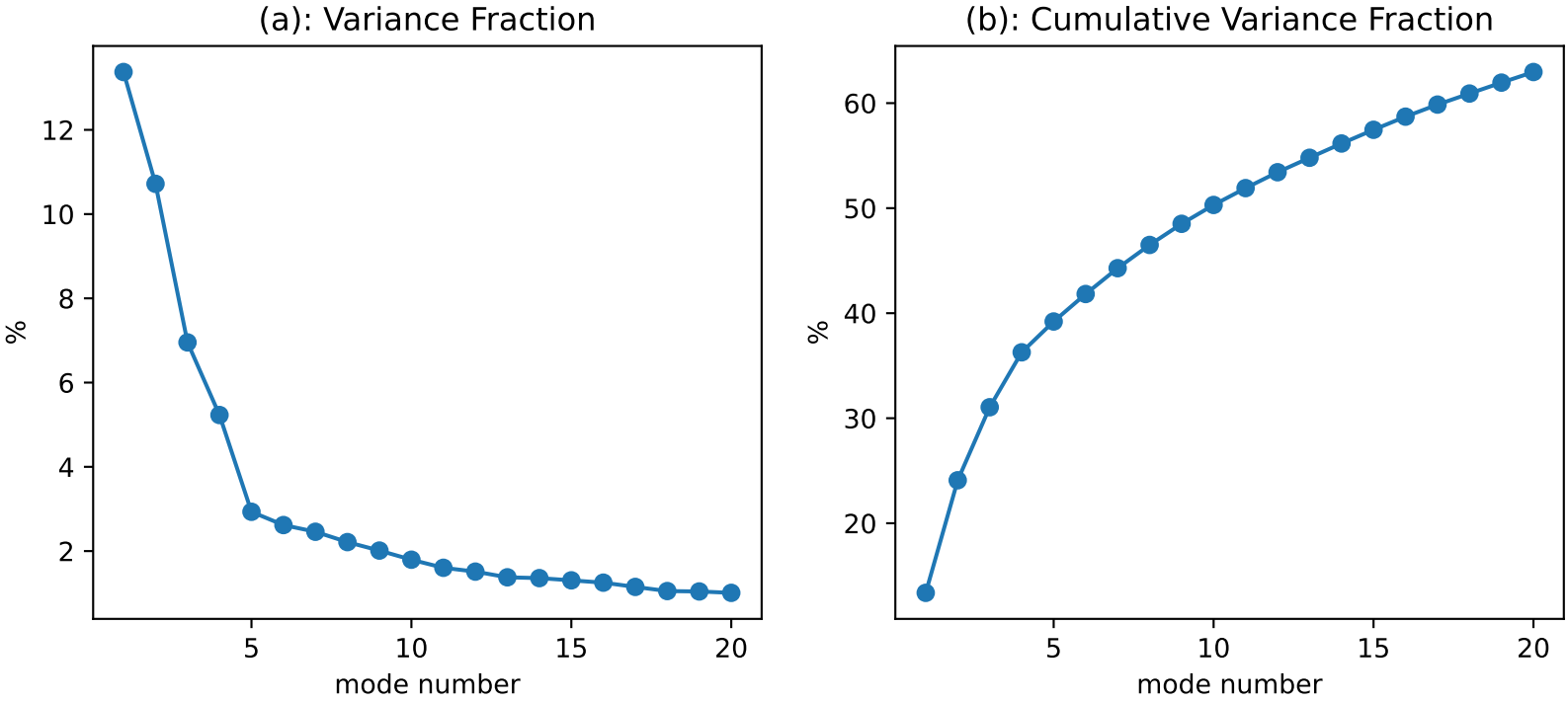
(a): Variance Fraction
%
mode number
(b): Cumulative Variance Fraction
%
mode number

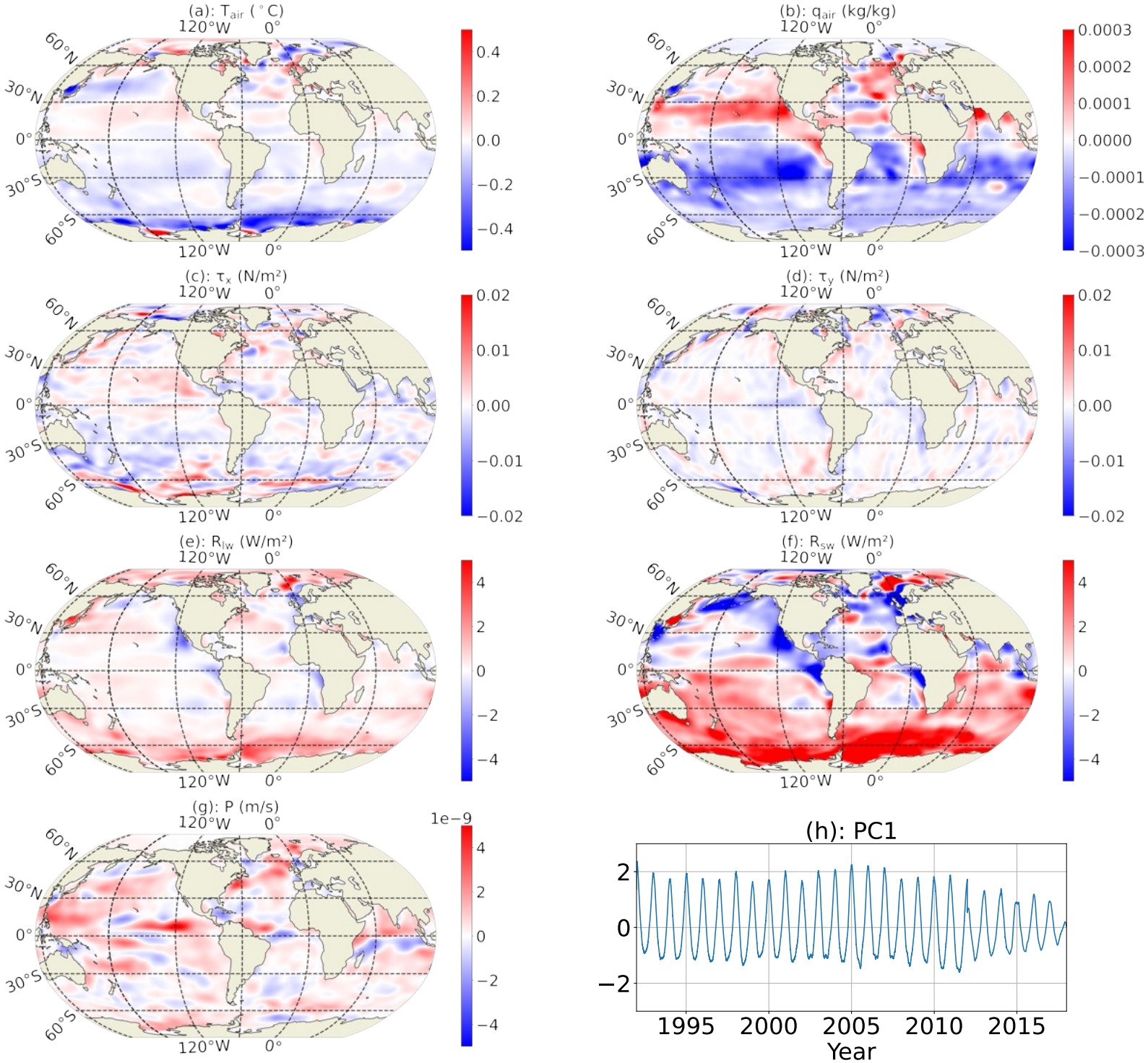
(a): T_{air} (°C)
(b): q_{air} (kg/kg)
(c): τ_x (N/m²)
(d): τ_y (N/m²)
(e): R_{lw} (W/m²)
(f): R_{sw} (W/m²)
(g): P (m/s)
1e−9
120°W
0°
60°N
30°N
0°
30°S
60°S
(h): PC1
Year
1995
2000
2005
2010
2015

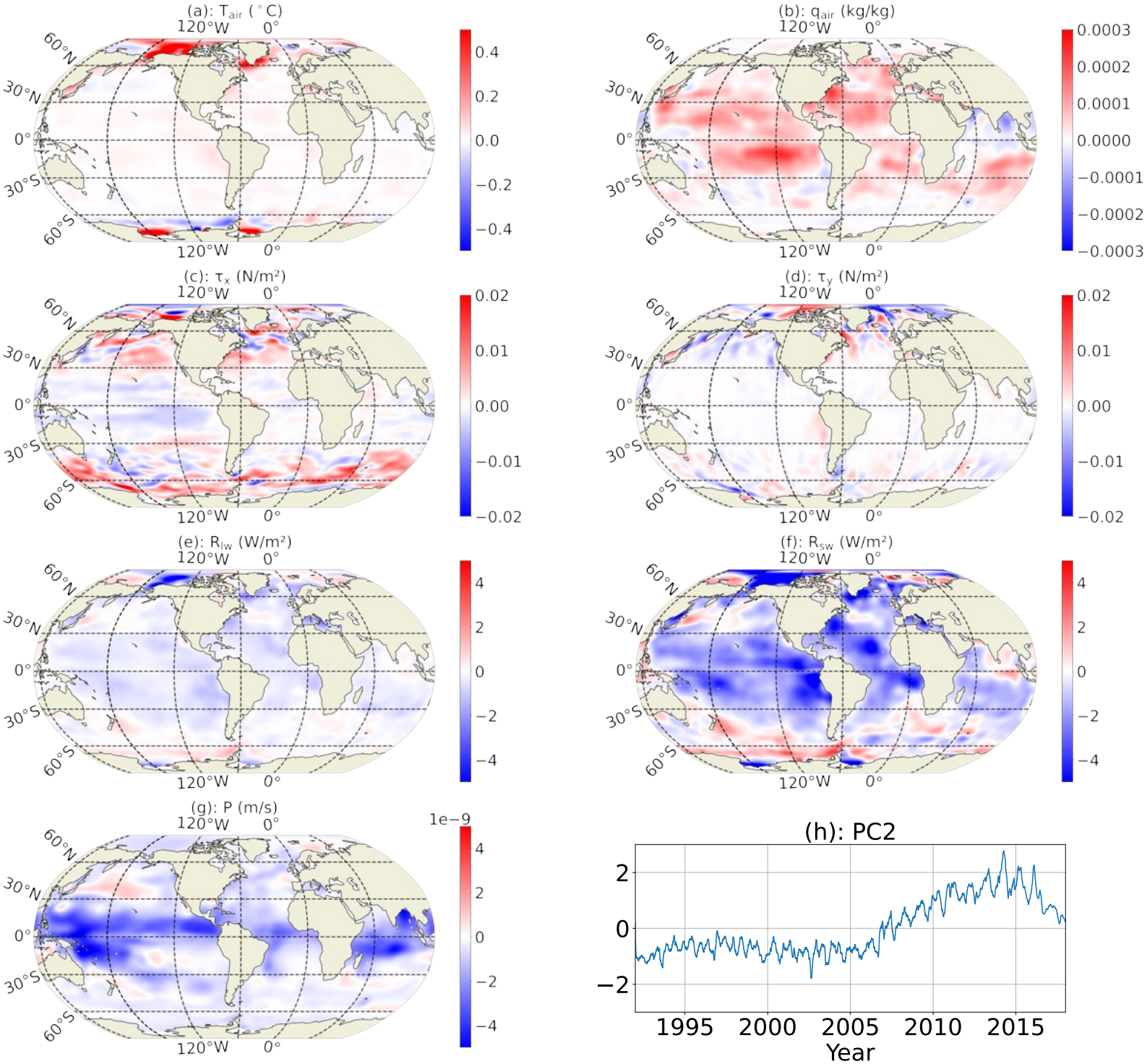
(a): T_{air} (°C)
(b): q_{air} (kg/kg)
(c): τ_x (N/m²)
(d): τ_y (N/m²)
(e): R_{lw} (W/m²)
(f): R_{sw} (W/m²)
(g): P (m/s)
1e−9
120°W
0°
60°N
30°N
0°
30°S
60°S
(h): PC2
Year
1995
2000
2005
2010
2015

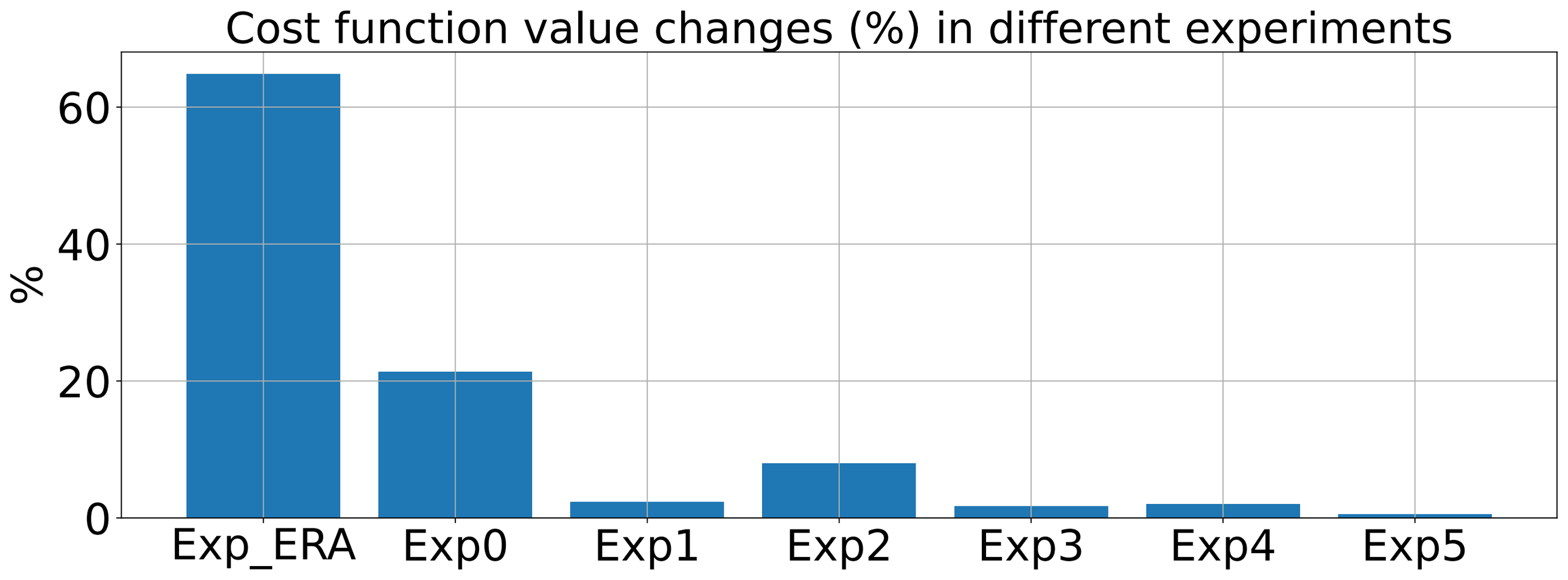
Cost function value changes (%) in different experiments
%
0
20
40
60
Exp_ERA
Exp0
Exp1
Exp2
Exp3
Exp4
Exp5

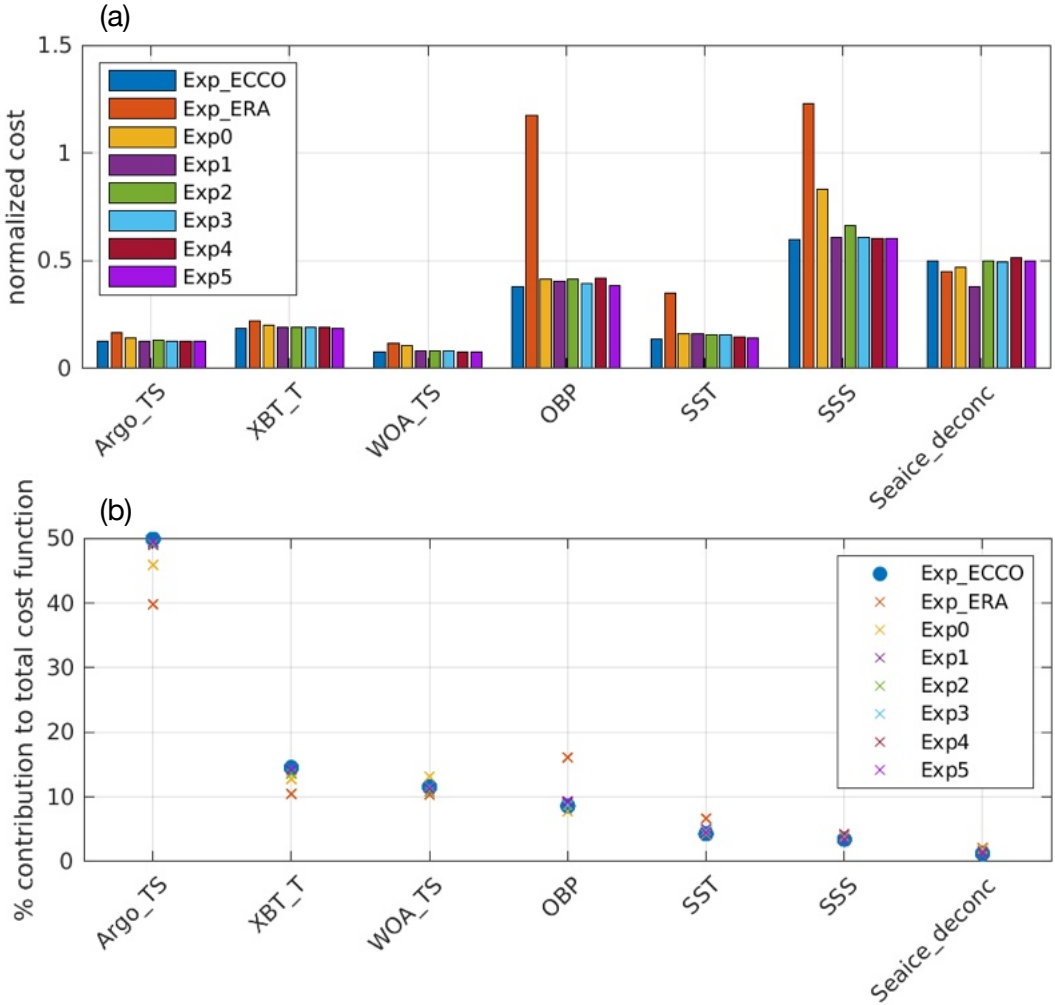
(a)
normalized cost
1.5
1
0.5
0
Exp_ECCO
Exp_ERA
Exp0
Exp1
Exp2
Exp3
Exp4
Exp5
Argo_TS
XBT_T
WOA_TS
OBP
SST
SSS
Seaice_deconc
(b)
% contribution to total cost function
50
40
30
20
10
0
Exp_ECCO
Exp_ERA
Exp0
Exp1
Exp2
Exp3
Exp4
Exp5
Argo_TS
XBT_T
WOA_TS
OBP
SST
SSS
Seaice_deconc

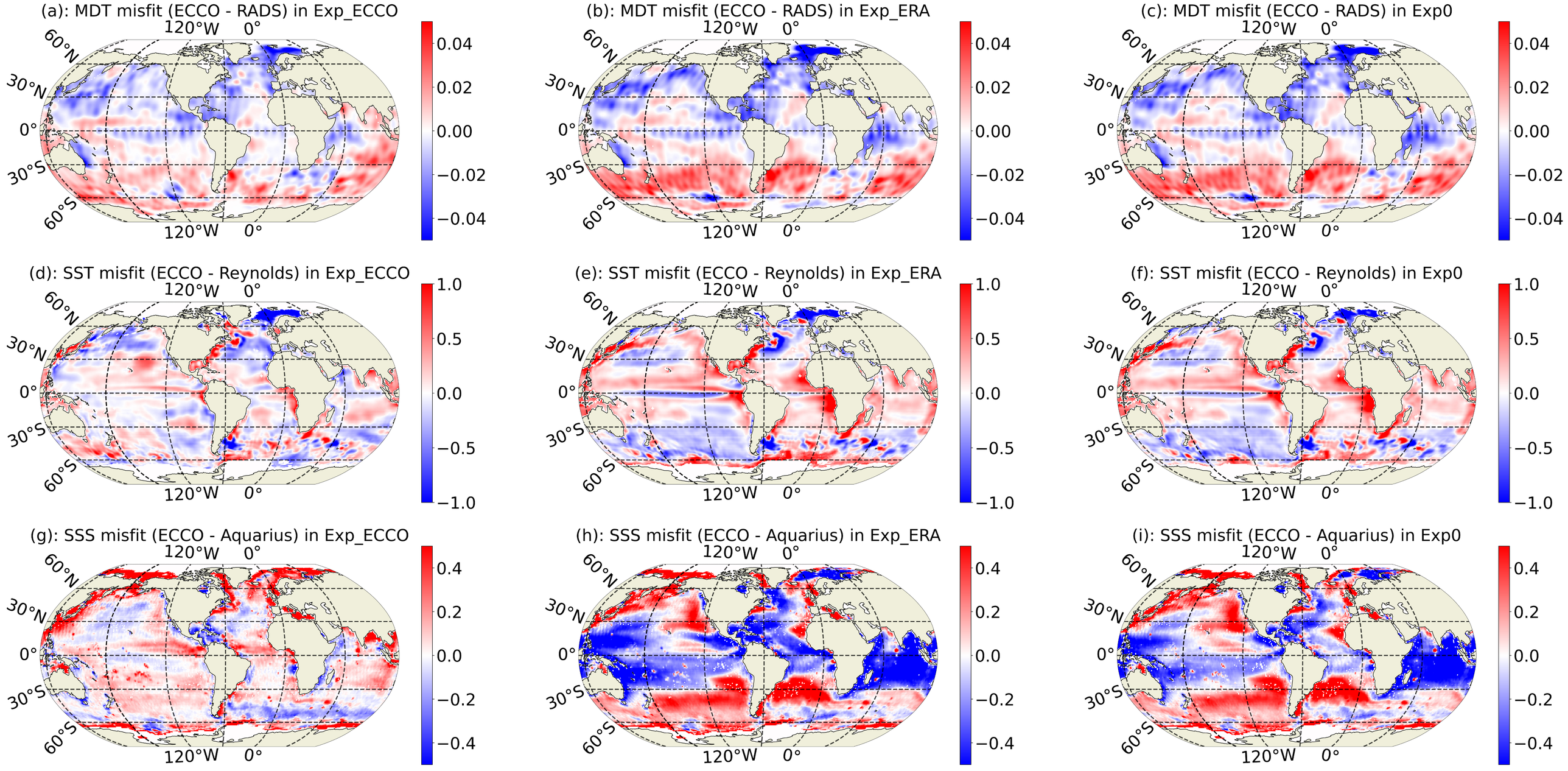
(a): MDT misfit (ECCO - RADS) in Exp_ECCO
(b): MDT misfit (ECCO - RADS) in Exp_ERA
(c): MDT misfit (ECCO - RADS) in Exp0
(d): SST misfit (ECCO - Reynolds) in Exp_ECCO
(e): SST misfit (ECCO - Reynolds) in Exp_ERA
(f): SST misfit (ECCO - Reynolds) in Exp0
(g): SSS misfit (ECCO - Aquarius) in Exp_ECCO
(h): SSS misfit (ECCO - Aquarius) in Exp_ERA
(i): SSS misfit (ECCO - Aquarius) in Exp0
120°W
0°
60°N
30°N
0°
30°S
60°S
0.04
0.02
0.00
−0.02
−0.04
1.0
0.5
0.0
−0.5
−1.0
0.4
0.2
0.0
−0.2
−0.4

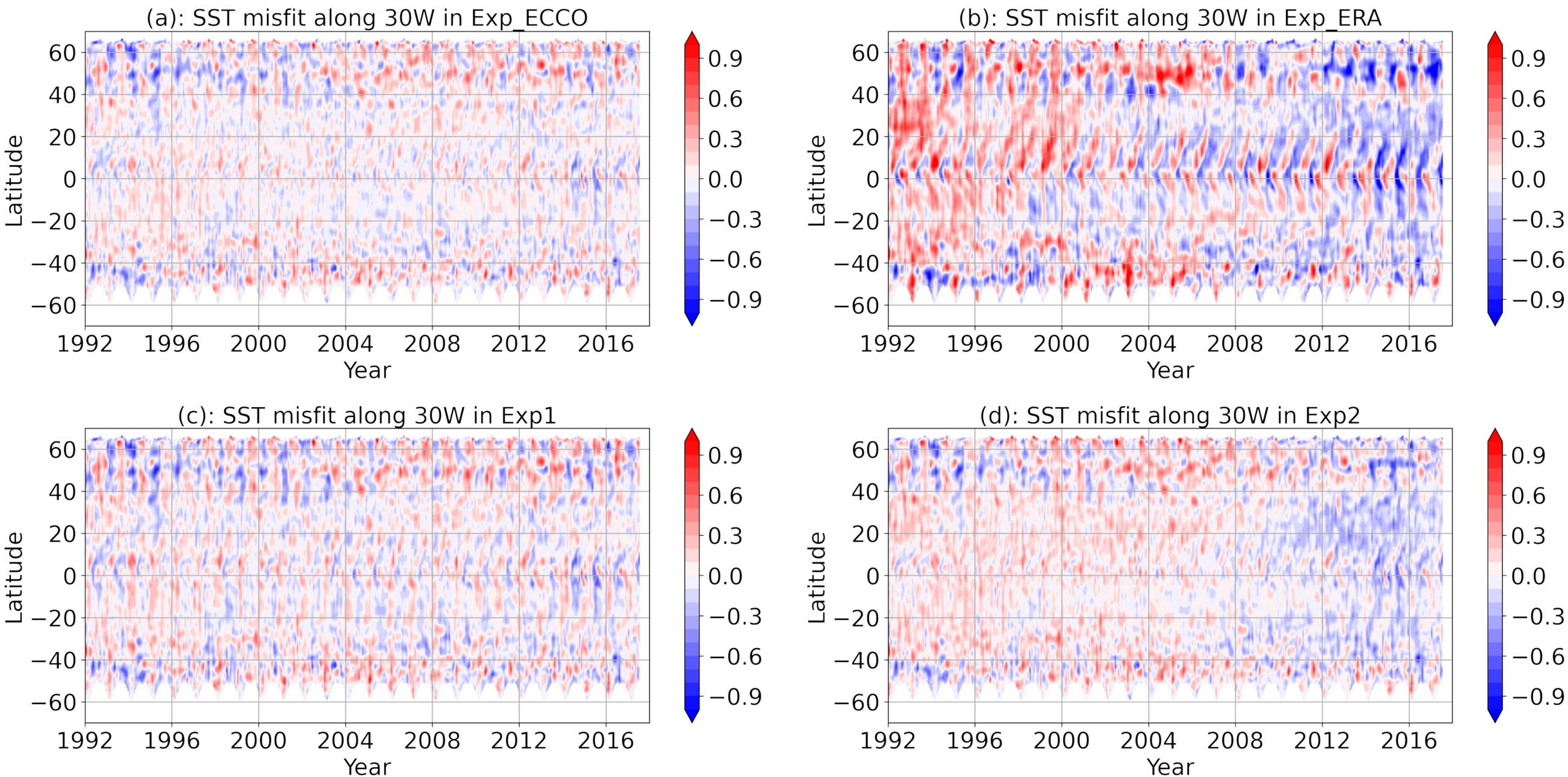
(a): SST misfit along 30W in Exp_ECCO
(b): SST misfit along 30W in Exp_ERA
(c): SST misfit along 30W in Exp1
(d): SST misfit along 30W in Exp2
Latitude
Year
60
40
20
0
−20
−40
−60
1992
1996
2000
2004
2008
2012
2016
0.9
0.6
0.3
0.0
−0.3
−0.6
−0.9

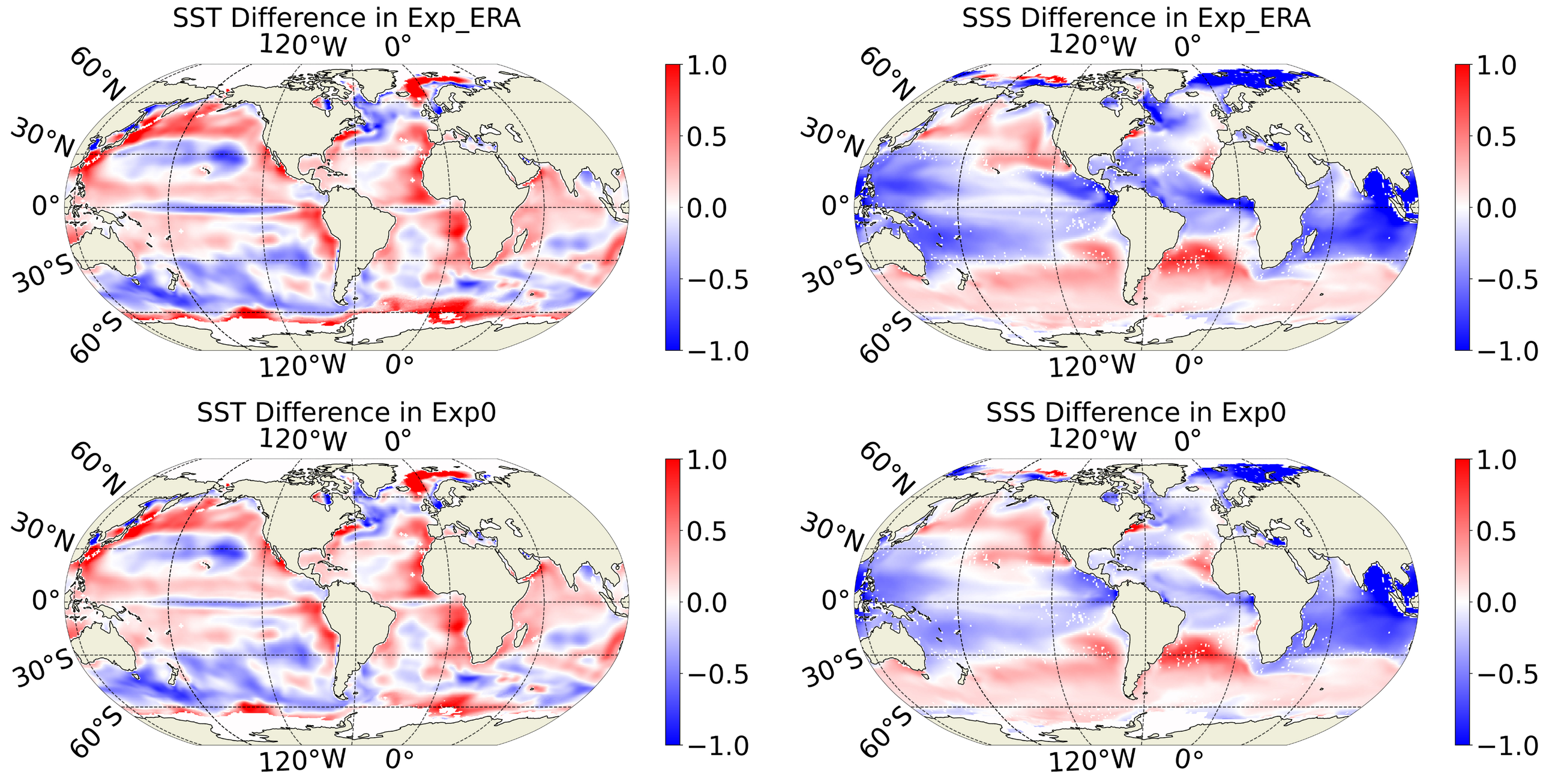
SST Difference in Exp_ERA
SSS Difference in Exp_ERA
SST Difference in Exp0
SSS Difference in Exp0
120°W
0°
60°N
30°N
0°
30°S
60°S
1.0
0.5
0.0
−0.5
−1.0

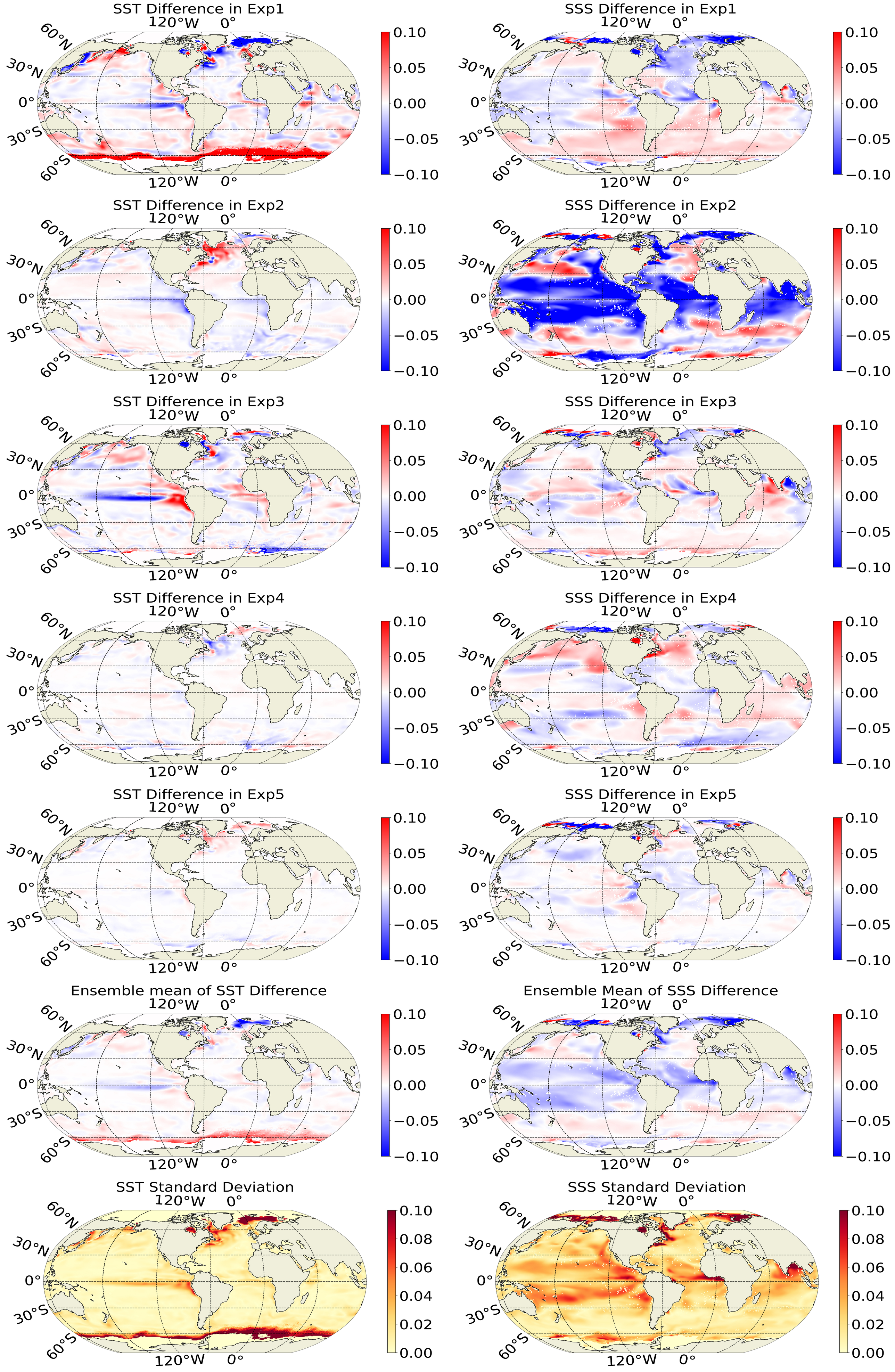
SST Difference in Exp1
SSS Difference in Exp1
SST Difference in Exp2
SSS Difference in Exp2
SST Difference in Exp3
SSS Difference in Exp3
SST Difference in Exp4
SSS Difference in Exp4
SST Difference in Exp5
SSS Difference in Exp5
Ensemble mean of SST Difference
Ensemble Mean of SSS Difference
SST Standard Deviation
SSS Standard Deviation
120°W
0°
60°N
30°N
0°
30°S
60°S
0.10
0.05
0.00
−0.05
−0.10
0.08
0.06
0.04
0.02
0.00

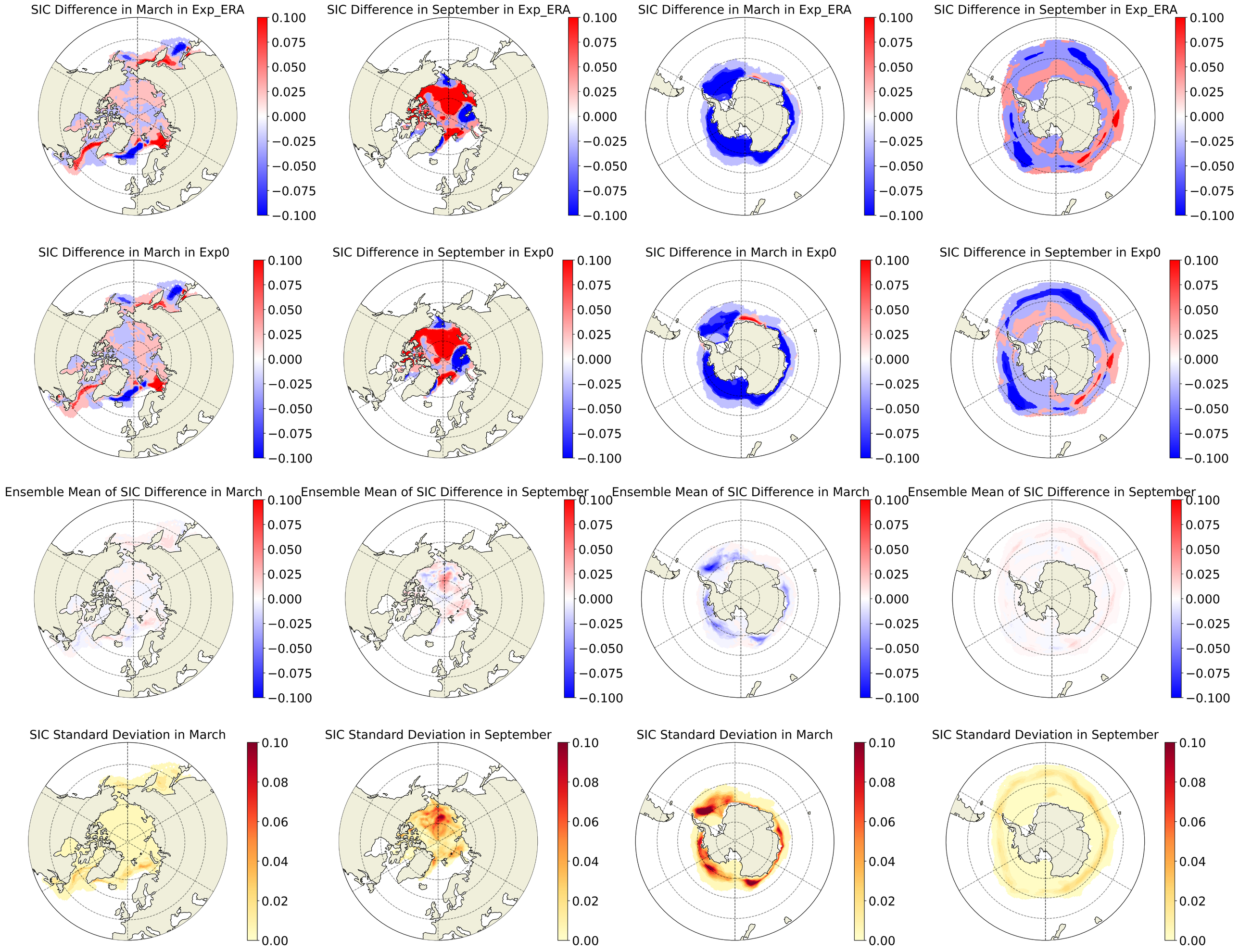
SIC Difference in March in Exp_ERA
SIC Difference in September in Exp_ERA
SIC Difference in March in Exp_ERA
SIC Difference in September in Exp_ERA
SIC Difference in March in Exp0
SIC Difference in September in Exp0
SIC Difference in March in Exp0
SIC Difference in September in Exp0
Ensemble Mean of SIC Difference in March
Ensemble Mean of SIC Difference in September
Ensemble Mean of SIC Difference in March
Ensemble Mean of SIC Difference in September
SIC Standard Deviation in March
SIC Standard Deviation in September
SIC Standard Deviation in March
SIC Standard Deviation in September
0.100
0.075
0.050
0.025
0.000
−0.025
−0.050
−0.075
−0.100
0.10
0.08
0.06
0.04
0.02
0.00

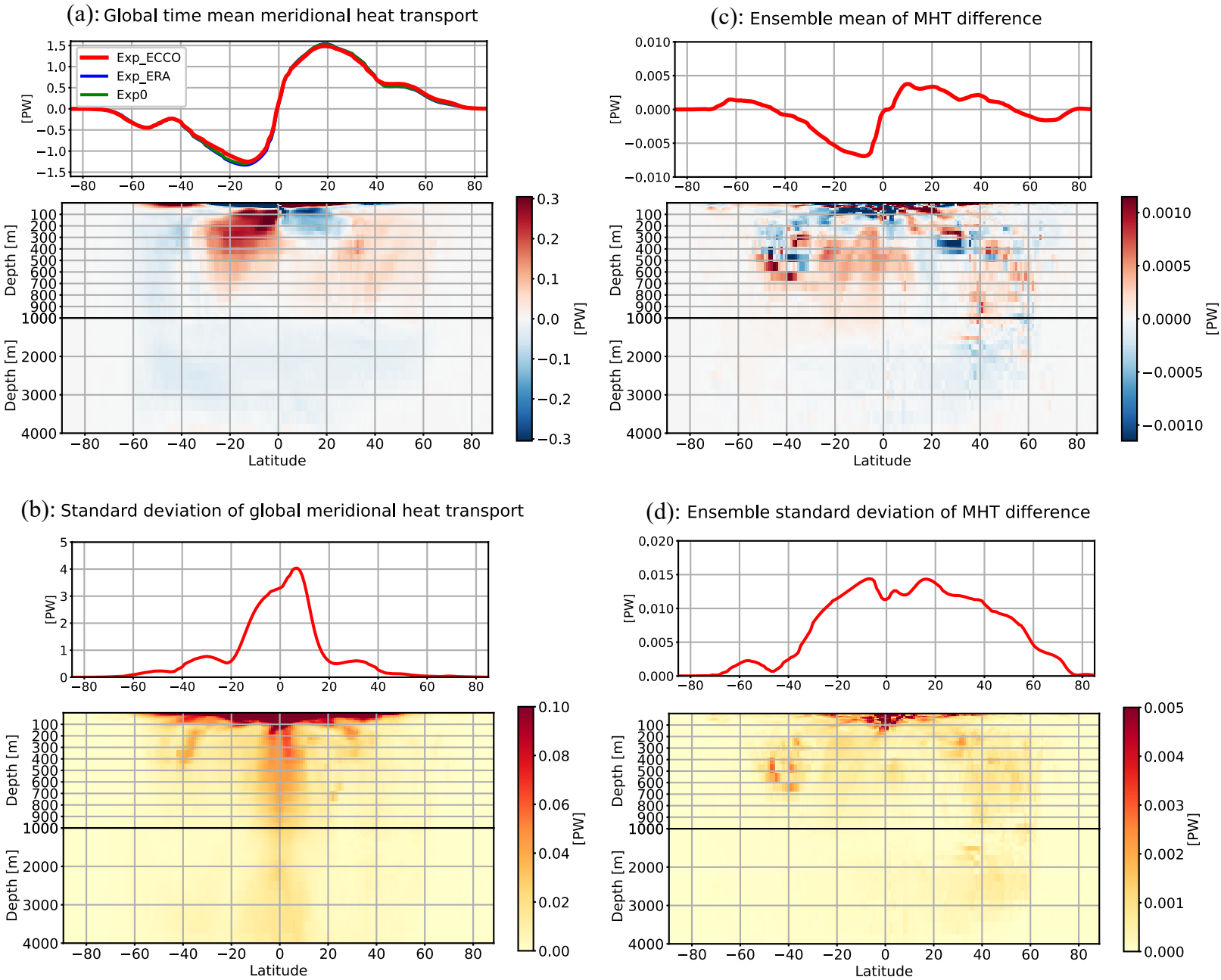
(a): Global time mean meridional heat transport
Exp_ECCO
Exp_ERA
Exp0
[PW]
Depth [m]
Latitude
(c): Ensemble mean of MHT difference
(b): Standard deviation of global meridional heat transport
(d): Ensemble standard deviation of MHT difference

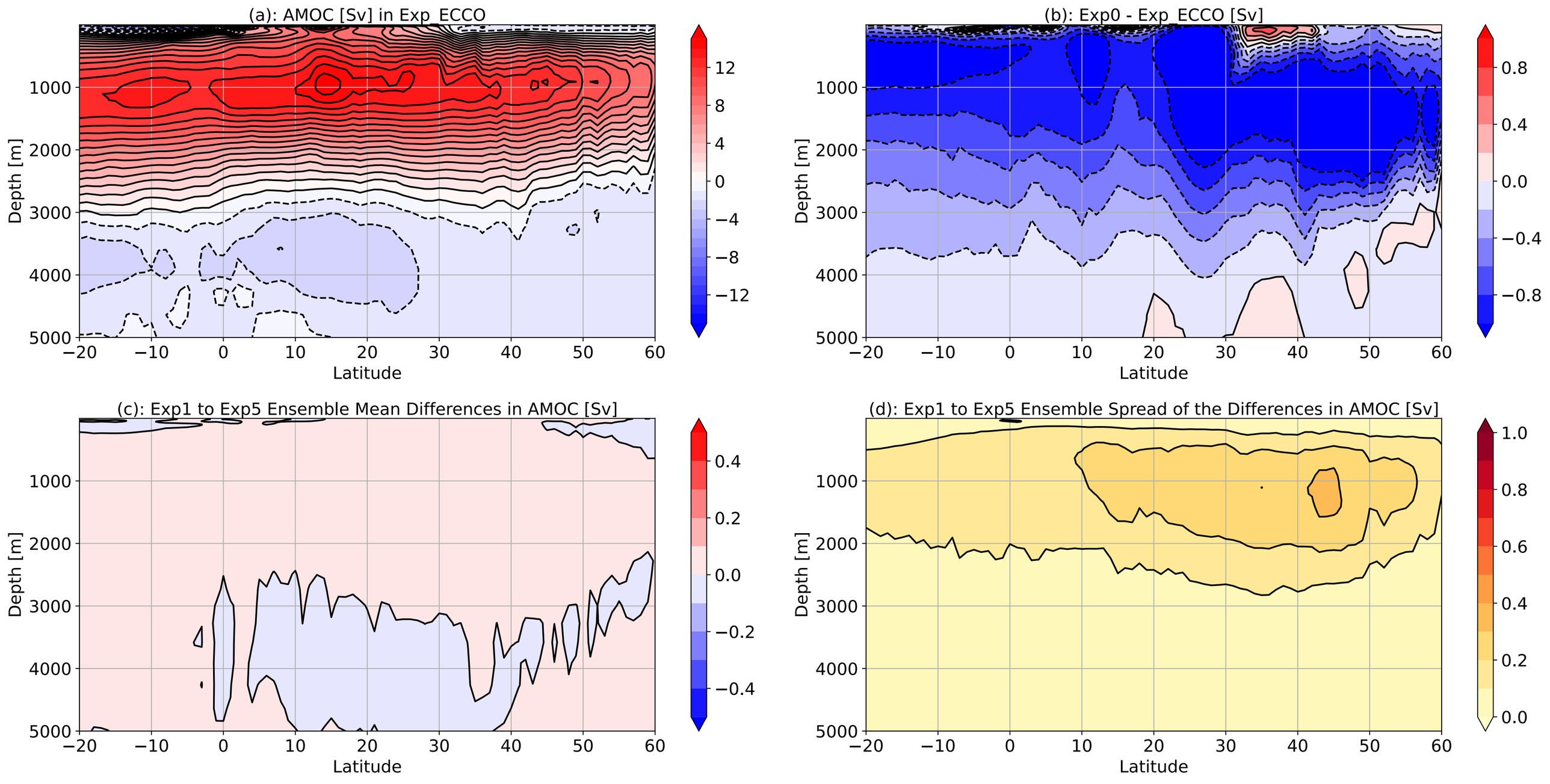
(a): AMOC [Sv] in Exp_ECCO
(b): Exp0 - Exp_ECCO [Sv]
(c): Exp1 to Exp5 Ensemble Mean Differences in AMOC [Sv]
(d): Exp1 to Exp5 Ensemble Spread of the Differences in AMOC [Sv]
Depth [m]
Latitude
1000
2000
3000
4000
5000
−20
−10
0
10
20
30
40
50
60
12
8
4
0
−4
−8
−12
0.8
0.4
0.0
−0.4
−0.8
0.4
0.2
0.0
−0.2
−0.4
1.0
0.8
0.6
0.4
0.2
0.0

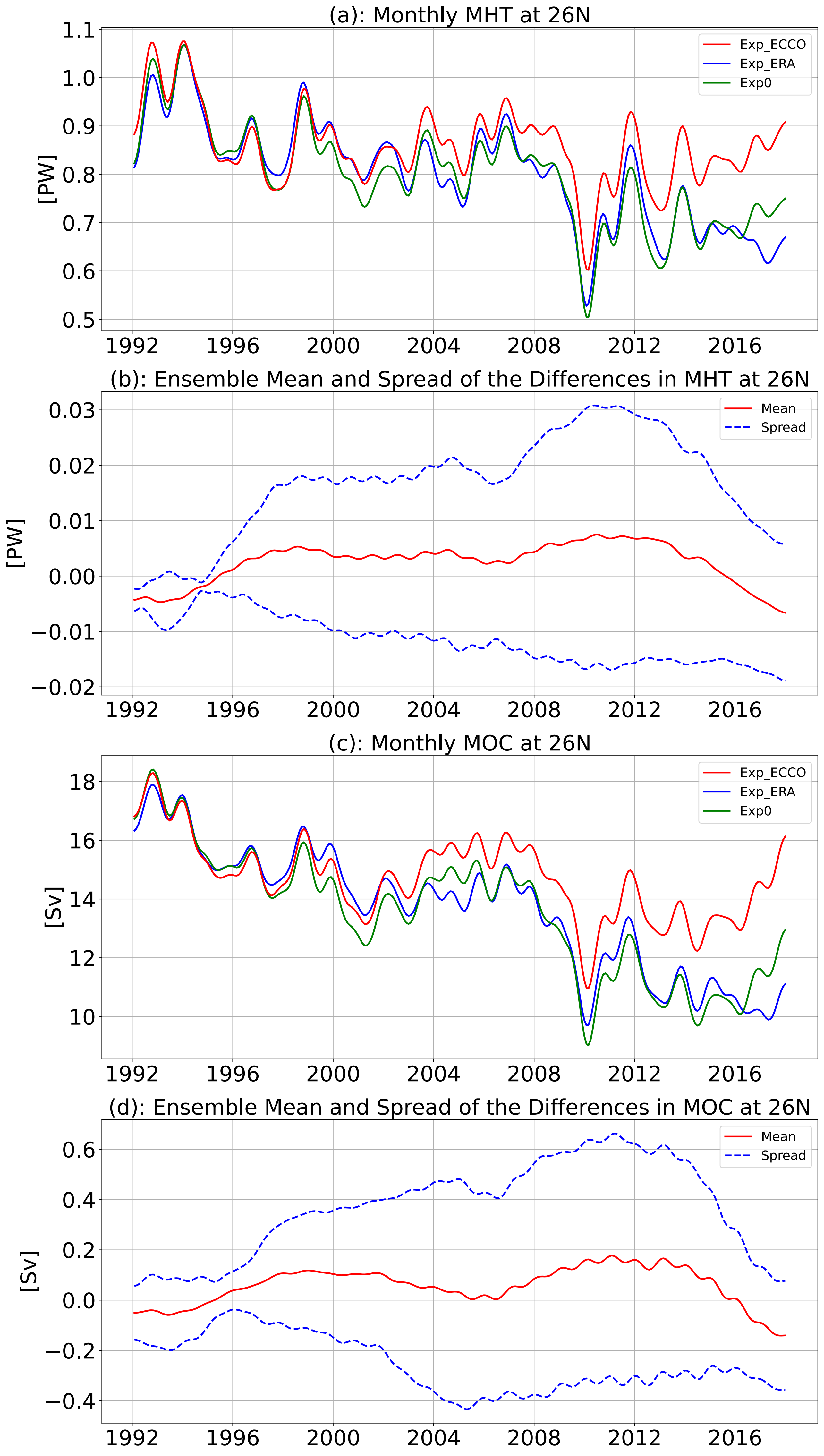
(a): Monthly MHT at 26N
[PW]
Exp_ECCO
Exp_ERA
Exp0
(b): Ensemble Mean and Spread of the Differences in MHT at 26N
[PW]
Mean
Spread
(c): Monthly MOC at 26N
[Sv]
Exp_ECCO
Exp_ERA
Exp0
(d): Ensemble Mean and Spread of the Differences in MOC at 26N
[Sv]
Mean
Spread

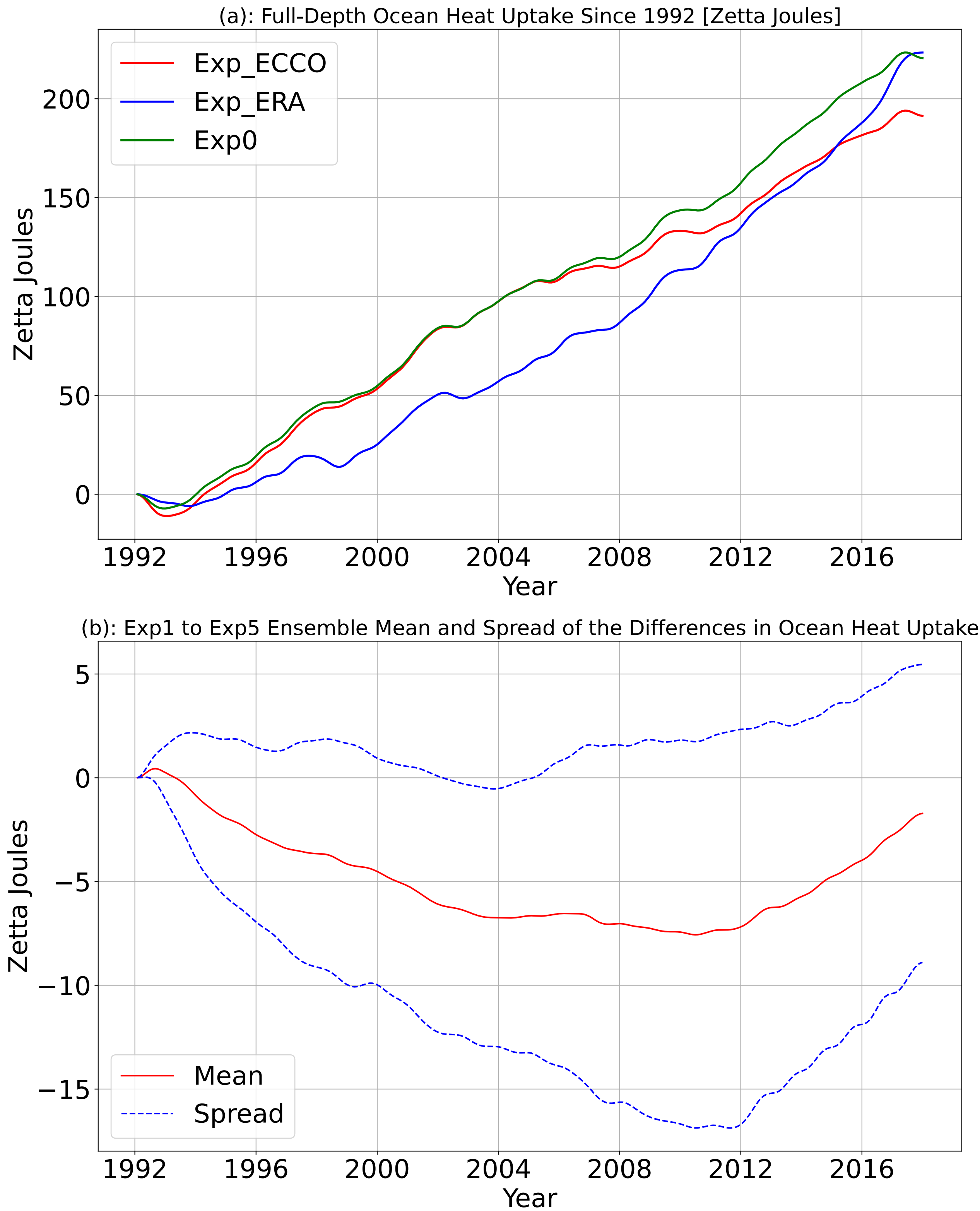
(a): Full-Depth Ocean Heat Uptake Since 1992 [Zetta Joules]
Exp_ECCO
Exp_ERA
Exp0
Zetta Joules
200
150
100
50
0
1992
1996
2000
2004
2008
2012
2016
Year
(b): Exp1 to Exp5 Ensemble Mean and Spread of the Differences in Ocean Heat Uptake
Zetta Joules
5
0
−5
−10
−15
Mean
Spread
1992
1996
2000
2004
2008
2012
2016
Year